J. Fluid Mech. (1999), *vol.* 390, *pp.* 93–126. Printed in the United Kingdom

© 1999 Cambridge University Press

Visualization and measurement of internal waves by 'synthetic schlieren'. Part 1. Vertically oscillating cylinder

By BRUCE R. SUTHERLAND†, STUART B. DALZIEL, GRAHAM O. HUGHES‡ AND P. F. LINDEN¶

Department of Applied Mathematics and Theoretical Physics, University of Cambridge, Silver Street, Cambridge, CB3 9EW, UK

(Received 4 April 1998 and in revised form 19 January 1999)

We present measurements of the density and velocity fields produced when an oscillating circular cylinder excites internal gravity waves in a stratified fluid. These measurements are obtained using a novel, non-intrusive optical technique suitable for determining the density fluctuation field in temporally evolving flows which are nominally two-dimensional. Although using the same basic principles as conventional methods, the technique uses digital image processing in lieu of large and expensive parabolic mirrors, thus allowing more flexibility and providing high sensitivity: perturbations of the order of 1% of the ambient density gradient may be detected. From the density gradient field and its time derivative it is possible to construct the perturbation fields of density and horizontal and vertical velocity. Thus, in principle, momentum and energy fluxes can be determined.

In this paper we examine the structure and amplitude of internal gravity waves generated by a cylinder oscillating vertically at different frequencies and amplitudes, paying particular attention to the role of viscosity in determining the evolution of the waves. In qualitative agreement with theory, it is found that wave motions characterized by a bimodal displacement distribution close to the source are attenuated by viscosity and eventually undergo a transition to a unimodal displacement distribution further from the source. Close quantitative agreement is found when comparing our results with the theoretical ones of Hurley & Keady (1997). This demonstrates that the new experimental technique is capable of making accurate measurements and also lends support to analytic theories. However, theory predicts that the wave beams are narrower than observed, and the amplitude is significantly under-predicted for low-frequency waves. The discrepancy occurs in part because the theory neglects the presence of the viscous boundary layers surrounding the cylinder, and because it does not take into account the effects of wave attenuation resulting from nonlinear wave–wave interactions between the upward and downward propagating waves near the source.

1. Introduction

In density-stratified environments internal gravity waves are a ubiquitous phenomenon that can transport momentum and energy through the fluid on relatively

† Present Address: Department of Mathematical Sciences, University of Alberta.
‡ Present Address: Research School of Earth Sciences, The Australian National University.
¶ Present Address: Department of Applied Mechanics and Engineering Science, UCSD.

fast time scales. Consequently, there have been a large number of studies devoted to understanding the mechanisms which are responsible for the generation, interaction and decay of internal waves. In atmospheric research, for example, it is important to develop predictive models of the amplitude of internal waves generated by wind flow over mountains because it is known that the momentum carried upward by the waves and deposited in the middle atmosphere is a significant source of drag that must be taken into account in order to reproduce the observed flow at these altitudes. Much of our understanding of the excitation and viscous attenuation of internal waves is based on linear theory, however, and the mechanism for coupling of internal waves with the source is poorly understood when the forcing amplitude is large. The aim of the current experimental study is to revisit the relatively simple flow studied by Mowbray & Rarity (1967), where internal waves are generated by oscillating a cylinder in a linear stratification. A new visualization and measurement technique enables us to assess quantitatively the effect of the source motion on the amplitude of excited internal wave modes, to examine the relative importance of weakly nonlinear wave–wave interactions, and to compare the observed rate of viscous attenuation of waves with theoretical predictions.

Small-amplitude monochromatic oscillations of a cylinder in a linear stratification were observed by Mowbray & Rarity (1967) to excite a 'St. Andrew's Cross' wave field, which consisted of four internal wave beams radiating from the cylinder at angles Θ to the vertical. We define the buoyancy frequency $N(z)$ for a stratified Boussinesq fluid as

$$N^2(z) = -\frac{g}{\rho_0}\frac{\mathrm{d}\rho}{\mathrm{d}z}, \tag{1.1}$$

where g is the gravitational acceleration, ρ_0 is a reference density, and $\rho(z)$ is the background density distribution as a function of height z. Then, if ω is the frequency of excitation, Θ is given by the dispersion relation,

$$\omega = N\cos\Theta, \tag{1.2}$$

as obtained from linear theory (e.g. Lighthill 1978; Voisin 1991) and is valid for $\omega < N$.

For a vibrating point source, linear theory predicts that inviscid fluid motion is aligned along beams of infinitesimal width (Makarov, Neklyudov & Chashechkin 1990). Thomas & Stevenson (1972) recognized that viscosity must reduce the shear to a finite value in this region and they produced a similarity solution describing the attenuation of motion with distance r along the beam from a virtual origin. Their prediction, that the beam width normal to the direction of motion scaled with $r^{1/3}$ and the fluid displacement along the beam with r^{-1}, was confirmed experimentally by Peters (1985). (Makarov *et al.* (1990) and Kistovich, Neklyudov & Chashechkin (1990) showed that the structure of the beams along which internal waves propagate was dependent upon the size of the source as well as the amplitude of oscillation. The beams produced by a finite-sized source were found to be of a comparable width to the source (Appleby & Crighton 1986, 1987; Voisin 1991; Hurley & Keady 1997). If the source size d was larger than the viscous scale

$$\ell_\nu = \frac{(g\nu)^{1/3}}{N}, \tag{1.3}$$

where ν is the kinematic viscosity, each beam appeared to consist of two bands which emanated from the tangential extremities of the source. Makarov *et al.* (1990)

and Kistovich *et al.* (1990) noted that this corresponds to a bimodal distribution of fluid displacement in the along-beam direction, with the maximum displacements occurring at the edges of the beam. When d is less than ℓ_v, viscosity was able to couple wave motion in the two bands across the width of the beam. If the coupling was sufficiently strong, this resulted in a unimodal displacement distribution in the along-beam direction, with the maximum displacement at the centre. By modelling the effect of dipole sources distributed on a circle of radius R, Makarov *et al.* (1990) predicted that wave beams with a bimodal structure close to the source would be attenuated by viscosity, and that the beams would have a unimodal structure for $r > R_v$, in which

$$R_v = \frac{g}{N^2} R^3/\ell_v^3 = \frac{NR^3}{\nu}. \tag{1.4}$$

For large r, however, the formulae used to estimate (1.4) may not be valid, and it is possible for the transition from bimodal to unimodal wave beam structures to occur over a much shorter distance than R_v. One result of our experiments is to show that R_v significantly overestimates the transition distance.

Full analytic solutions of the approximate equations describing internal waves generated by oscillating cylinders were found by Hurley & Keady (1997). The equations were derived on the basis of linear theory using the 'boundary layer approximation' of Thomas & Stevenson (1972), and their solutions qualitatively reproduced the near-cylinder bimodal and far-field unimodal structures of the wave beams. However, it is not known with what accuracy this approximation models the coupling between the waves and the source. Specifically, because their theory neglects the viscous boundary layer which in reality surrounds the cylinder, it remains to be determined what effect this layer has on the wave beam width and amplitude. Our experiments are used to test the Hurley & Keady (1997) theory and to examine where the theory may be improved.

In most previous experimental studies of internal wave fields, schlieren techniques have been used qualitatively to visualize the flow (e.g. Mowbray & Rarity 1967; Thomas & Stevenson 1972). More recently, Peters (1985) and Merzkirch & Peters (1992) made use of interferometric techniques to visualize the wave field produced by an oscillating cylinder. The latter study also demonstrated that the associated velocity field could be measured using particle image velocimetry techniques. Here we employ a novel optical technique related to the classical schlieren method but which overcomes many of the financial and practical limitations associated with both schlieren and interferometry.

When light waves pass through a medium in which the index of refraction varies, the ray path is bent by refraction and undergoes a phase change compared with waves in a homogeneous medium. Optical techniques may be used to detect the deflection or phase changes, and from this the changes in the refractive index and density fields may be inferred. These techniques fall into three broad categories. The classical shadowgraph method (Dvorak 1880) is sensitive to the curvature in the refractive index field which focuses or defocuses nominally parallel light rays. This technique is essentially qualitative because it is difficult to extract quantitative information about the density fluctuations, partly because of the need to specify an appropriate boundary condition at the edges of the field of view. Interferometry (Mach & von Weltrubsky 1878) provides direct measurements of variations in the speed of light (and hence density) through the phase change experienced by monochromatic light. However, its application is often limited by the cost and precision required in setting

it up. Schlieren methods (Toepler 1864) are sensitive to refractive index variations in the plane normal to light rays passing through the medium. In this paper we shall concentrate on a variant of the last of these, a technique we refer to hereafter as 'synthetic schlieren'. A thorough review of all three classes of techniques may be found in Merzkirch (1974).

While schlieren has been used for many years to visualize flows containing variations in refractive index, its application has often been limited by the expense of the optical components (especially if visualization of a large region is required) and through difficulty in extracting quantitative measurements. In its simplest form, the intensity of a 'knife edge' schlieren image is modulated in proportion to gradients of the refractive index perturbations in the direction chosen by the orientation of the knife edge. Variants of this schlieren technique exist that colour code the refractive index gradients or which are sensitive to the magnitude of the gradients in the plane normal to the light rays.

A number of recent advances have been reported in the use of schlieren techniques to visualize the density gradient field in stratified flows. Irvin & Ross (1991) used a linear photodiode array to overcome the common problem of making high-accuracy intensity measurements of images produced by knife-edge schlieren methods. This approach was used to infer the density profile in convection experiments. Greenberg, Klimek & Buchele (1995) described a colour-schlieren technique which overcomes the need to measure intensities, the changes in refractive index gradient within the flow instead appearing as different hues in the image. They used a colour CCD array and a video digitizer to make experimental measurements of a temperature field. The schlieren techniques described thus far resolve only those density gradients which are effectively normal to the knife edge or to colour gradations. One solution to this problem is the four-colour schlieren system developed by Scheitle & Wagner (1990), capable of measuring the density gradient in any direction.

The principles behind synthetic schlieren and how these may be used to extract information about the density gradients and its time derivative are outlined in § 2. We believe that synthetic schlieren overcomes many of the disadvantages of more traditional methods outlined above. In particular, synthetic schlieren is relatively easy to use and may be scaled up to visualize large regions of the flow. Setting up synthetic schlieren is also much simpler than for the Moiré fringe method where the precise alignment of two masks is required. Synthetic schlieren is particularly advantageous in that it can be used to make non-intrusive quantitative measurements of the full wave field continuously in time, although this is possible only if the flow is nominally two-dimensional.

Here, with the aid the synthetic schlieren technique, new insight is attained into the problem of internal wave generation by a circular cylinder oscillating vertically at a range of different amplitudes and frequencies. In § 3 we summarize the recent theory of Hurley & Keady (1997), and in § 4 we compare the theoretically predicted characteristics of the waves with those found in our experiments. Although the predicted wave structure is similar to observations, there are consistent discrepancies between the predicted and observed amplitudes: theory generally under-predicts the wave-beam width, and the predicted amplitude is significantly smaller than the observed amplitude for waves with a frequency small compared with the buoyancy frequency. We explain that this discrepancy occurs, in part, because the viscous boundary layer surrounding the oscillating cylinder is neglected by the theory, and because nonlinear interactions between upward and downward propagating wave

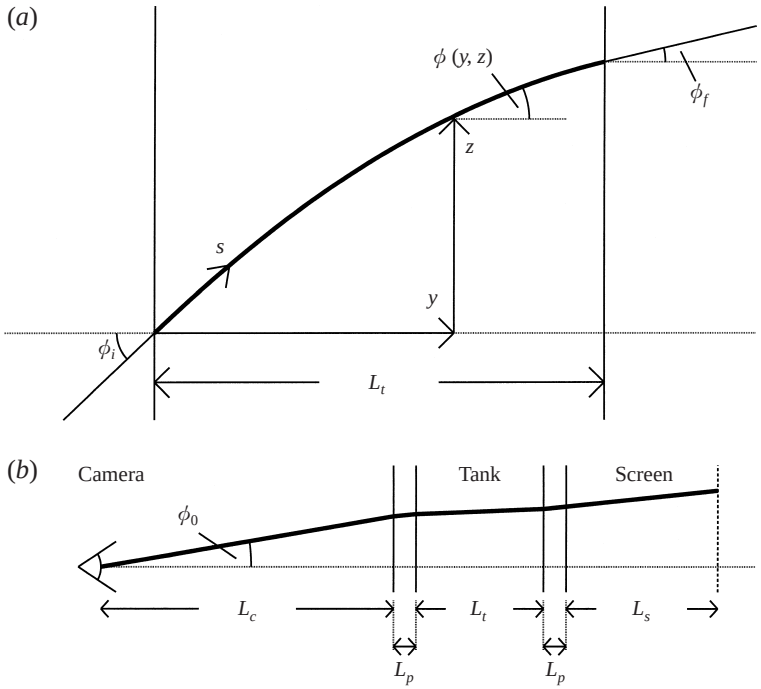

FIGURE 1. (*a*) Schematic showing the curved path of a light ray passing through linearly stratified fluid, and (*b*) the complete path of a light ray from a screen to a camera passing through a tank filled with stratified fluid. Here the screen is a back-illuminated grid of horizontal lines.

beams radiating from the source enhance the beam attenuation. In § 5 we present conclusions and discuss implications of this work for future research.

2. Synthetic schlieren

When internal gravity waves propagate in a stratified fluid, isopycnal surfaces are displaced, resulting in regions where the local density gradient is either increased or decreased relative to the background gradient. As will be shown in this section, the path of a nearly horizontal light ray through stratified fluid is deflected due to changes in the refractive index gradient. We make use of the fact that the density and refractive index of a salt solution follow an almost linear relationship (Weast 1981), and by measuring the deflection of light rays passing through the solution, the fluctuation in the density gradient may be calculated. Ultimately this leads to a measure of the amplitude of the internal gravity waves.

2.1. *Theoretical determination of internal wave field*

Consider the path followed by a light ray incident with an upward inclination upon a spanwise cross-section of a tank filled with salt-stratified water, as shown in figure 1(*a*). For clarity, the curvature of the ray through the tank in the figure is exaggerated from the relatively small curvature that occurs in a typical experiment. Because the index of refraction increases with salinity, the ray is refracted so that the angle of the ray above the horizontal decreases. The path taken by a ray of light satisfies Snell's Law,

$$n \cos \phi = \text{constant}, \tag{2.1}$$

in which $n = n(x, y, z)$ is the index of refraction of the medium and $\phi = \phi(x, y, z)$ is the angle the light ray makes with surfaces of constant n, where z is the height, x is the distance along the tank, and y is the spanwise distance across the tank. We introduce the along-ray coordinate s and decompose this into coordinates parallel ($s_\parallel$) and perpendicular ($s_\perp$) to surfaces of constant n. Differentiating (2.1) with respect to s, and noting that $\mathrm{d}s_\parallel/\mathrm{d}s = \cos\phi$ and $\mathrm{d}s_\perp/\mathrm{d}s = \sin\phi$, we obtain

$$\frac{\partial n}{\partial s_\perp}\cos\phi\sin\phi - n\sin\phi\frac{\mathrm{d}\phi}{\mathrm{d}s} = 0. \tag{2.2}$$

Eliminating $\mathrm{d}\phi/\mathrm{d}s$ using $\mathrm{d}^2 s_\perp/\mathrm{d}s_\parallel{}^2 = \sec^3\phi\,\mathrm{d}\phi/\mathrm{d}s$ gives

$$\frac{\mathrm{d}^2 s_\perp}{\mathrm{d}s_\parallel{}^2} = \frac{\sec^2\phi}{n}\frac{\partial n}{\partial s_\perp}. \tag{2.3}$$

We may ignore the along-ray variation in both ϕ and n provided $\partial n/\partial s_\perp$ remains finite and $|\mathrm{d}s_\perp/\mathrm{d}s_\parallel| \ll 1$, and thus integrate (2.3) using their values at the point of entry of the light ray into the tank.

For two-dimensional flows of the form considered in this paper, spanwise variations in the refractive index are ignored ($n = n(x, z)$) and $s_\parallel$ coincides with the cross-tank coordinate y. Furthermore, the condition $|\mathrm{d}s_\perp/\mathrm{d}s_\parallel| \ll 1$ linearizes (2.3), thus allowing us to identify $s_\perp$ with either x or z to form two independent equations:

$$\frac{\mathrm{d}^2 x}{\mathrm{d}y^2} = \frac{\sec^2\phi_{ix}}{n_i}\frac{\partial n}{\partial x}, \tag{2.4}$$

$$\frac{\mathrm{d}^2 z}{\mathrm{d}y^2} = \frac{\sec^2\phi_{iz}}{n_i}\frac{\partial n}{\partial z}, \tag{2.5}$$

where ϕ_{ix} and ϕ_{iz} are the angles that the incident light ray makes to the y-axis in the horizontal and vertical directions, respectively, and n_i is the index of refraction where the ray is incident. For the remainder of this paper we shall consider only the vertical deflection of the light rays as described by (2.5). Moreover the experimental arrangement will be such that $|\phi| < 5^\circ$ and $\sec^2\phi_{iz}$ may be taken as unity.

Except where strong mixing or layering occurs, it is valid to assume that the refractive index varies linearly over the small depth traversed by the light ray (typically less than 1 cm), allowing us to replace the vertical gradient in n with the squared buoyancy frequency N^2 at the same level using the relationship

$$\frac{\partial n}{\partial z} = \frac{\mathrm{d}n}{\mathrm{d}\rho}\frac{\partial \rho}{\partial z} = -\left(\frac{1}{g}\frac{\rho_0}{n_0}\frac{\mathrm{d}n}{\mathrm{d}\rho}\right)n_0 N^2. \tag{2.6}$$

Here ρ_0 and n_0 are reference values of the density and index of refraction, respectively. Because $\mathrm{d}n/\mathrm{d}\rho$ is approximately constant for salt-water solutions (Weast 1981), we write

$$\frac{\partial n}{\partial z} = -n_0\gamma N^2, \tag{2.7}$$

where

$$\gamma = \frac{1}{g}\frac{\rho_0}{n_0}\frac{\mathrm{d}n}{\mathrm{d}\rho} \simeq 1.878\times 10^{-4}\ \mathrm{s}^2\ \mathrm{cm}^{-1}. \tag{2.8}$$

Substituting (2.7) into (2.5) and integrating gives

$$z(y) = z_i + y\tan\phi_{iz} - \tfrac{1}{2}\gamma N^2 y^2, \tag{2.9}$$

where z_i is the vertical position of the incident light ray.

Therefore, the effect of stable stratification is to bend a nearly horizontal light ray along a (concave downward) parabolic arc. This has two important consequences: the stratification acts to shift the ray downward and the angle of propagation changes. We take advantage of this optical effect to determine the refractive index gradients. Synthetic schlieren measures the intensity change of parts of an image in a manner similar to the classical schlieren method. The experimental set-up and accuracy of this approach is discussed in §§ 2.4 and 2.5. In a related novel approach, which we refer to as 'pattern matching refractometry', the apparent motion of a random array of dots are used to determine the density gradient field. This technique, which is more closely akin to particle image velocimetry, will be discussed in detail in future work (Dalziel, Hughes & Sutherland 1999).

Quantitative measurements are obtained using synthetic schlieren by modelling the effect of changes in the refractive index gradient on a light ray passing at angles close to the horizontal through stratified fluid. A typical experimental set-up is illustrated in figure 1(*b*). The schematic shows a light ray starting at the image screen, a distance L_s behind the rear Perspex tank wall. This ray first passes through the Perspex wall before being deflected by refractive index gradients within the body of the fluid. On exiting the fluid it passes through the second Perspex wall ultimately entering the video camera at an angle ϕ_0 above the horizontal.

Repeated application of Snell's Law together with (2.9) gives the total vertical deflection of a light ray travelling from the image screen to the camera as

$$\begin{aligned} z(N^2,\phi_0) \simeq\ & L_c\phi_0 \\ & +L_p\left(n_a/n_p\right)\phi_0 \\ & +L_t\left(n_a/n_w\right)\phi_0 \quad -\tfrac{1}{2}\gamma N^2 L_t^2 \\ & +L_p\left(n_a/n_p\right)\phi_0 \quad -L_p\left(n_w/n_p\right)\gamma N^2 L_t \\ & +L_s\phi_0 \qquad\quad -L_s\left(n_w/n_a\right)\gamma N^2 L_t, \end{aligned}$$

in which n_a, n_w, and n_p are the refractive indices of air, water and Perspex, taken to be 1, 1.333 and 1.49, respectively, and we have taken $\tan\phi \simeq \phi$. Subscripts c, t and s denote camera, tank and screen, respectively.

If the isopycnal surfaces are locally perturbed by internal gravity waves, then N^2 is changed and a light ray passing through the wave field is deflected. In particular, the light ray entering the camera at an angle ϕ_0 from the horizontal originates from a different location on the screen. The apparent displacement, Δz, of the image is given by

$$\begin{aligned} \Delta z(\Delta N^2,\phi_0) \simeq\ & -\frac{1}{2}\gamma\Delta N^2 L_t^2 \\ & -L_p\left(n_w/n_p\right)\gamma\Delta N^2 L_t - L_s\left(n_w/n_a\right)\gamma\Delta N^2 L_t, \end{aligned} \tag{2.10}$$

which may be rearranged to give the perturbation to the squared buoyancy frequency in terms of the vertical displacement:

$$\Delta N^2 \simeq -\Delta z\frac{1}{\gamma}\left[\tfrac{1}{2}L_t^2 + L_t n_w\left(\frac{L_p}{n_p}+\frac{L_s}{n_a}\right)\right]^{-1}. \tag{2.11}$$

For the experiments reported in this paper, $L_t = 20.0\,\text{cm}$, $L_p = 1.5\,\text{cm}$, and $L_s = 34.2\,\text{cm}$. Substituting into (2.11) gives $\Delta N^2 \simeq -0.2\Delta z$ where N^2 and Δz are measured

in s^{-2} and cm, respectively. Discussion on how the apparent vertical displacement Δz of a light ray can be determined is deferred until § 2.2.

Once the ΔN^2 field is known, we may construct the perturbation density field ρ' and the vertical displacement field ζ'. Assuming $|\zeta'|$ is small compared to the vertical wavelength of the internal waves,

$$\rho'(x,z) = -\frac{\rho_0}{g}\int \Delta N^2 \,\mathrm{d}z, \tag{2.12}$$

and

$$\zeta'(x,z) = -\frac{1}{N^2}\int \Delta N^2 \,\mathrm{d}z. \tag{2.13}$$

The constants of integration are obtained from boundary conditions specific to the geometry of the wave field. For example, in regions unaffected by the waves ρ' and ζ' are set to zero.

In addition, we may calculate a finite difference approximation to the time derivative of the squared buoyancy frequency $(N^2)_t$ by determining Δz at successive times spaced at intervals much less than the period of the wave motion. Assuming incompressibility and an approximately linear background stratification, and provided the amplitude of the waves is not too large, $(N^2)_t$ can be used to construct the perturbation horizontal velocity field, u', and vertical velocity field w':

$$u'(x,z) = \frac{1}{N^2}\int (N^2)_t \,\mathrm{d}x, \tag{2.14}$$

and

$$w'(x,z) = -\frac{1}{N^2}\int (N^2)_t \,\mathrm{d}z. \tag{2.15}$$

The constants of integration in this case may again be determined by suitable choice of boundary conditions.

2.2. *Optical arrangement*

Figure 2 compares typical experimental set-ups for the classical schlieren, Moiré fringe and synthetic schlieren methods. The light rays represented by solid lines in each diagram indicate their path in the absence of density perturbations ($\Delta N^2 = 0$). Dotted and dashed lines indicate their path when perturbations result in a decrease and increase, respectively, of ΔN^2. Recall from (2.10) that the deflection of a light ray relative to the path taken in the absence of any density perturbations is upwards when $\Delta N^2 < 0$ and downwards when $\Delta N^2 > 0$. Classical schlieren relies on perturbations to the density field altering the passage of the light rays relative to the knife edge so that a greater or lesser fraction of the light is blocked by the knife edge. With the orientation of the edge as shown in figure 2(*a*), the amount of light reaching the screen is increased for $\Delta N^2 > 0$ and decreased when $\Delta N^2 < 0$. The Moiré fringe method operates in a similar manner, but replaces the pair of parabolic mirrors and knife edge by a pair of accurately aligned masks. These masks consist of a set of parallel lines and are normally aligned so that 50% of the light passing through the first mask is stopped by the second mask. Due to camera parallax, the lines on the mask in front of the tank are more closely spaced than those to the rear of the tank. For the relative positions of the masks illustrated in figure 2(*b*), the mean intensity of the light, averaged over a scale larger than the spacing of the lines on the masks, is again increased for $\Delta N^2 > 0$ and decreased when $\Delta N^2 < 0$. The Moiré

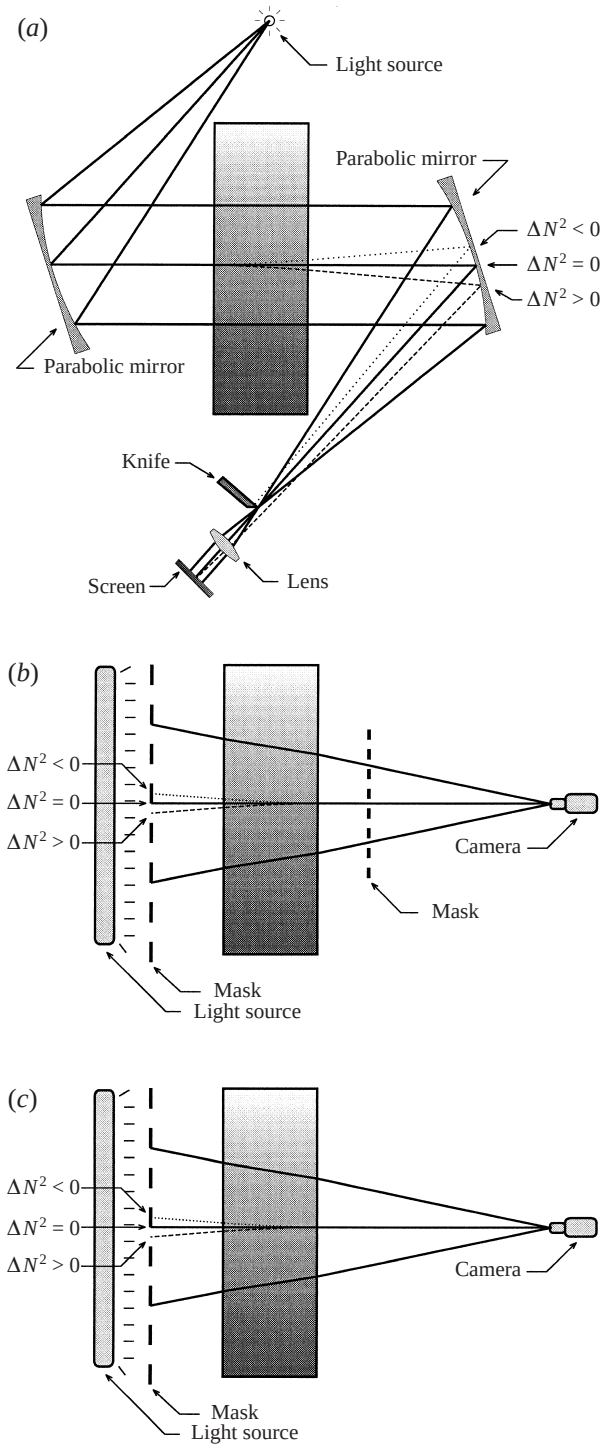

FIGURE 2. Schematics showing three different experimental set-ups using the schlieren technique for internal gravity wave visualization.

fringe method is cheaper to implement and may be scaled up to cover larger domains more readily than classical schlieren because expensive parabolic mirrors are not required. The main difficulty is that the alignment between the apparent position of the mask behind the tank and the analysing mask in front of the tank is critical and non-trivial, especially if light entering the camera is not approximately parallel or if the stratification is nonlinear so that the line spacings are not related by a simple scale factor. The synthetic schlieren method overcomes this difficulty by replacing the analysing mask used in the Moiré fringe method with one that is digitally generated.

In the simplest (qualitative) mode of synthetic schlieren operation, a digitized image of the mask behind the tank is captured when density perturbations in the flow are absent. If the intensity field for this unperturbed image is described by $I(x_p, z_p)$ and the intensity field for a perturbed image is $I'(x_p, z_p)$, then it is a simple matter to construct

$$P_{abs}(x_p, z_p) = \alpha |I' - I|, \tag{2.16}$$

where α is some gain factor and x_p, z_p are the (integer) horizontal and vertical pixel coordinates, respectively, of the image. Ideally, the image I is a sequence of perfectly 'black' ($I = I_{black}$) and perfectly 'white' ($I = I_{white}$) horizontal lines on alternate rows of pixels. In general, however, it is not possible to align the mask and pixels in the camera with sufficient precision to obtain this idealized sequence of lines. Even if such an alignment was possible, blurring and distortion by the camera optics and the CCD array in the video camera would lead to the contrast being reduced. Typically, therefore, the separation between successive 'white' and 'black' lines on the mask is arranged to be approximately 5 pixels. In order to minimize the effect of horizontal jitter in the timing of the video signal, the camera is always oriented so that the scan lines are parallel with the lines on the mask and thus the system will be sensitive to 'vertical' fluctuations (in the camera's frame of reference).

The definition of P_{abs} in (2.16) is convenient because it can be calculated in real time over the full field while an experiment is in progress. However, it does not indicate whether the light rays are deflected upward or downward. To do this in the simplest possible way we define

$$P_{sign}(x_p, z_p) = \text{sign}(\partial I/\partial z)\alpha(I' - I). \tag{2.17}$$

This expression is evaluated only where the finite difference approximation to $|\partial I/\partial z|$ based on neighbouring rows of pixels is sufficiently large. In § 2.3 we shall discuss in more detail how an accurate quantitative measure of ΔN^2 may be obtained from the image pair $I(x_p, z_p)$ and $I'(x_p, z_p)$.

2.3. *Quantitative measurements*

In order to determine the apparent vertical displacement field Δz (and hence ΔN^2), it is necessary to consider how the digitized images $I(x_p, z_p)$ and $I'(x_p, z_p)$ are related. We confine our attention to the apparent vertical displacement of nominally horizontal lines: apparent horizontal displacement of these lines cannot be detected. If the intensity measured by the pixel at (x_p, z_p) is initially $I(x_p, z_p)$, and the subsequent apparent vertical displacement in pixel coordinates is Δz_p, then the new intensity measured by that same pixel is

$$I'(x_p, z_p) \approx I(x_p, z_p - \Delta z_p). \tag{2.18}$$

Here we have neglected the effect of curvature in the refractive index field so that to first order the camera detects a digitized intensity field which has been translated

locally by a fractional vertical pixel displacement Δz_p. Equation (2.18) could be expanded as a Taylor series to compute Δz_p, but in practice the local variation of pixel intensity with z_p is found to be almost linear. Therefore, it is computationally more efficient to suppose that Δz_p (and hence Δz) can be represented locally by a quadratic in I':

$$\Delta z = (z_{-1} - z_0)\frac{(I' - I_0)(I' - I_1)}{(I_{-1} - I_0)(I_{-1} - I_1)} + (z_1 - z_0)\frac{(I' - I_0)(I' - I_{-1})}{(I_1 - I_0)(I_1 - I_{-1})}. \tag{2.19}$$

Here we have made the transformation from pixel intensity to real space coordinates, and I_{-1}, I_0 and I_1 are short-hand for $I(x_p, z_p - 1)$, $I(x_p, z_p)$ and $I(x_p, z_p + 1)$, respectively. The vertical coordinates of the pixels in real space are taken to be z_{-1}, z_0 and z_1, respectively. We solve (2.19) only if $I_1 < I_0 < I_{-1}$ or $I_{-1} < I_0 < I_1$, and the intensity contrast across the three lines is sufficiently large: $|I_1 - I_{-1}| > \Delta I_{\min}$, in which the threshold $\Delta I_{\min}$ is set explicitly.

Once Δz has been determined, (2.11) is applied to determine ΔN^2. Points for which Δz could not be calculated are replaced by the weighted average of surrounding values that have been determined. Specifically, a Gaussian weighting is used such that its magnitude is greatest at the location of the pixel being determined. Finally, the resulting image of ΔN^2 is filtered in the Fourier domain to reduce noise and systematic errors. The accuracy of the result is discussed in § 2.5.

2.4. *Experimental set-up*

Here we describe how the synthetic schlieren technique can be set up for a typical laboratory experiment, giving details of the image processing system and the particular experiments used to visualize internal gravity waves.

Figure 2(*c*) shows a schematic diagram (not to scale) of the arrangement of the experimental apparatus for synthetic schlieren. A video camera (COHU 4910 Series High Performance monochrome CCD) is focused through the tank of stratified fluid upon the back-illuminated image screen. The camera is positioned as far as practicable in front of the tank ($\simeq$ 350 cm) in order to minimize parallax error, while ensuring the region of interest in the flow, typically 25 cm in the vertical by 30 cm in the horizontal, fills the field of view. With this arrangement, light rays enter the camera at angles up to 1.7° from an axis normal to the tank wall. Thus, a light ray originating from the upper or lower extremities of the field of view traverses through a depth of approximately 0.5 cm of fluid as it passes through the tank.

To detect accurately the apparent displacement of light rays, the image screen must consist of fine details on a high-contrast background. We have used a variety of back-illuminated screens composed of horizontal black lines, a regular array of dots and a random array of dots. Following the approach outlined in the previous subsections, we shall restrict our attention to images produced using horizontal lines. Back-lighting is provided by several fluorescent tubes so as to make the illumination as uniform as possible. Lines of width 0.2 cm are laser-printed at 0.4 cm intervals onto translucent paper (tracing paper) or onto transparencies that are positioned on top of translucent paper. The CCD camera is focused upon the image screen so that the intensity contrast between the centre of the black lines and the back-illuminated spaces between the lines is maximized.

The basic components in the image processing system are the CCD camera and a computer (IBM compatible PC with 90 MHz Pentium Processor) fitted with a frame-grabber card (Data Translation DT2862). The frame-grabber produces an eight-bit digitized image with a spatial resolution of 512×512 pixels. The intensity assigned to

an individual pixel represents the average intensity over its area (typically 0.01 cm^2). The digitized intensities are then manipulated by computer using the software package DigImage (Dalziel 1992).

For all experiments reported here, the tank is filled with salt-stratified water to a depth of approximately 35 cm using the standard 'double-bucket' method. The density variation is approximately linear with depth and is characterized by the buoyancy frequency $N \simeq 1.0 \pm 0.05\,s^{-1}$. In most experiments we examine the generation of waves by a vertically oscillating cylinder oriented with its axis horizontal and spanning the width of the tank. The cylinder radius is $R = 1.67$ cm. The cylinder is suspended from its centre by a supporting rod, the opposite end of which is positioned along a 45 cm arm. The rod is driven in an oscillatory fashion by an eccentric cam from a speed-controlled servo motor. The maximum amplitude (half the peak to peak displacement) of oscillation is 0.32 cm, or approximately 20% of the cylinder radius. To ensure the cylinder motion is vertical, the top of the supporting rod is hinged and the rod itself is confined to pass through a rigid guide. The cylinder is located approximately 12 cm above the bottom of the tank. An angled barrier spanning the width of the tank is positioned nearby to block waves reflected from the bottom of the tank, but the barrier is not so close that it interferes with wave generation near the cylinder.

2.5. *Experimental accuracy*

The accuracy of synthetic schlieren depends upon the experimental set-up. It is sensitive to the distance between the tank and the grid, the tank width, the pixel resolution of the camera, and the distance and intensity contrast between successive light and dark grid lines. In the set-up of the experiments reported here, the image recorded by a single pixel typically spans a vertical distance of 0.1 cm, and the intensity contrast between light and dark lines is approximately 100 out of a full range of 256. Thus, applying (2.19), we find that apparent displacements of grid lines can be detected to a resolution of 1/25 of the pixel spacing, or approximately 0.004 cm. Putting this value in (2.11), it is found that changes in ΔN^2 as small as $0.0008\,s^{-2}$ can be detected under ideal conditions, a fraction of a percent of the background squared buoyancy frequency. From linear theory for plane internal gravity waves propagating in a background where $N^2 \simeq 1\,s^{-2}$, it can be shown that vertical displacements as small as 0.0001 of the vertical wavelength can be detected.

Unfortunately thermal noise in the laboratory environment induces refractive index variations in the air between the camera and the image screen rendering this ideal limit inaccessible much of the time. The synthetic schlieren data for these experiments is filtered to reduce sources of error, in particular fluctuations due to rapid air temperature variations in the vicinity of the experiment. These variations typically evolve over shorter time scales than those associated with the internal wave motions. Therefore, the effect of the former can be reduced by applying a low-pass filter in time to the time series of ΔN^2 obtained from vertical cross-sections of the flow. After filtering we find that changes in ΔN^2 can be detected over background noise for values as small as $0.002\,s^{-2}$. Quantitative measurements, though less accurate, nonetheless provide remarkable sensitivity. Tests in a different experimental set-up where the densities were measured simultaneously by a conductivity probe and synthetic schlieren helped to confirm the small magnitude of this error. The tests were also used to determine the appropriate value for $\Delta I_{\min}$ and assess its control of the errors. If the wave motion is well resolved, averaging over many pixels can give substantially narrower error bars. At any particular point, after filtering out noise

and locally averaging, the technique generally gives measurements accurate to $0.01\,\mathrm{s}^{-2}$. For the oscillating cylinder experiments presented here, the ΔN^2 field associated with large-amplitude waves can be as large as $0.2\,\mathrm{s}^{-2}$, and corresponding measurements are therefore accurate to within 5% of actual values.

3. Theory of internal waves generated by an oscillating cylinder

Approximate theoretical solutions for inviscid (Hurley 1997) and viscously attenuating (Hurley & Keady 1997) internal waves generated by oscillating elliptical cylinders have been derived. For the special case of viscously attenuating waves generated by a vertically oscillating circular cylinder the solutions may be compared directly with experimental measurements. Here we briefly review the results, introducing somewhat different notation than that employed by Hurley & Keady (1997), and we comment upon approximations made in the theory in anticipation of discrepancies observed between theory and experiment.

It is assumed that the cylinder is oscillating in a uniformly stratified fluid with buoyancy frequency N, and that the vertical velocity of the cylinder in time is given by $W\exp(-\mathrm{i}\omega t)$. The resulting two-dimensional wave motion is given in terms of the streamfunction $\psi(x,z)\exp(-\mathrm{i}\omega t)$, such that the velocity field is

$$u = -\frac{\partial\psi}{\partial z}\mathrm{e}^{-\mathrm{i}\omega t}, \quad w = \frac{\partial\psi}{\partial x}\mathrm{e}^{-\mathrm{i}\omega t}. \tag{3.1}$$

The Boussinesq approximation is employed. It is supposed that the flow is laminar everywhere and that no flow separation occurs, and it is assumed the waves are of small amplitude so that linear theory applies. That is, it is assumed that $A/R \ll 1$, in which R is the cylinder radius. Then $\psi(x,z)$ satisfies

$$N^2\frac{\partial^2\psi}{\partial x^2} - \omega^2\nabla^2\psi + \mathrm{i}\omega\nu\nabla^4\psi = 0, \tag{3.2}$$

in which ν is the kinematic viscosity.

Solutions are found in a coordinate system with axes aligned in the along-beam (r) and across-beam (σ) directions. For the wave beam propagating upward and to the right of the source we take

$$\sigma = -x\cos\Theta + z\sin\Theta, \quad r = x\sin\Theta + z\cos\Theta, \tag{3.3}$$

in which $\Theta = \cos^{-1}(\omega/N)$ is the angle of the wave beam with the vertical. In this coordinate system positive values of σ correspond to the upper flank of the wave beam. The equations in this coordinate system are simplified by applying the 'boundary-layer approximation' (Thomas & Stevenson 1972) which assumes that the derivatives with respect to σ are everywhere much larger than those with respect to r. Thus, the following equation is derived:

$$-\frac{\partial^2\psi}{\partial\sigma\partial r} + \frac{\mathrm{i}\nu}{2\omega\tan\Theta}\frac{\partial^4\psi}{\partial\sigma^4} = 0. \tag{3.4}$$

It is also assumed that

$$\lambda = \frac{\nu}{2R^2\omega\tan\Theta} \tag{3.5}$$

is small so that the thickness of the boundary layer surrounding the cylinder is small compared to R. Then the solution to (3.4) for the right and upward propagating wave

beam is given by

$$\psi = -\frac{\mathrm{i}WR}{2}\mathrm{e}^{\mathrm{i}\Theta}\int_0^\infty \frac{J_1(K)}{K}\exp\left(-K^3\lambda\frac{r}{R} - \mathrm{i}K\frac{\sigma}{R}\right)\mathrm{d}K, \quad r > 0, \tag{3.6}$$

where J_1 is the first-order Bessel function of the first kind (Hurley & Keady 1997). For the beams in the other three quadrants similar solutions exist which for the vertically oscillating cylinder may be determined from (3.6) using straightforward symmetry arguments. If $\psi_{\mathrm{R}+}(\equiv\psi)$, $\psi_{\mathrm{R}-}$, $\psi_{\mathrm{L}+}$ and $\psi_{\mathrm{L}-}$ are the streamfunctions corresponding to the wave beams in the upper right, lower right, upper left and lower left quadrants, respectively, then $-\psi_{\mathrm{L}+}(-x,z) = -\psi_{\mathrm{L}-}(-x,-z) = \psi_{\mathrm{R}-}(x,-z) = \psi_{\mathrm{R}+}(x,z)$. The full solution is the superposition of the streamfunction of each of the four beams. The result exhibits an even reflection symmetry about the x-axis and an odd reflection symmetry about the z-axis. The existence of this symmetry is demonstrated and the constructive and destructive interference of the upward and downward propagating beams to the right of the cylinder is analysed in detail in the Appendix.

Far from the source where the overlap between any two beams is negligible, it is sufficient to consider the structure of one beam alone. For comparison with experiments, we wish to find the solution for $\Delta N^2(x,z)$. Using linear theory, we see that

$$\Delta N^2 = \frac{-\mathrm{i}}{\omega}N^2\frac{\partial^2\psi}{\partial x\partial z}. \tag{3.7}$$

Hence

$$\Delta N^2 = -\frac{WRN^2}{2\omega}\mathrm{e}^{\mathrm{i}\Theta}\left[\int_0^\infty \left(-\tfrac{1}{2}(\lambda^2k^4R^4+1)k^2\sin 2\Theta + \mathrm{i}\lambda k^4R^2\cos 2\Theta\right)\frac{J_1(Rk)}{k}\exp(-R^2k^3\lambda r - \mathrm{i}k\sigma)\,\mathrm{d}k\right], \tag{3.8}$$

where we have defined $k = K/R$. For fixed values of r, this integral is solved using a discrete fast Fourier transform algorithm (Press *et al.* 1993, § 12.2).

The approximations leading to (3.4) are applicable for internal waves far from the source. If, as is true in the case of the experiments presented here, the boundary layer surrounding the cylinder has non-negligible thickness, then near the source the amplitude of the internal waves may be sufficiently large that linear theory does not apply. It is well known, for example, that for inviscid waves ($\nu = 0$) the streamfunction is singular along tangents to the cylinder oriented at an angle Θ to the vertical. The inviscid theory therefore predicts unphysically large velocities along these tangents (although the width of this region is infinitesimally thin). If viscous effects are not neglected, the Hurley & Keady (1997) theory nonetheless predicts unphysically large velocities close to the source, specifically for $|\sigma| \simeq R$ and $r \ll R(1/\lambda(2\pi)^3)$. For typical experiments reported here, this occurs if $r \ll 0.5R$, which is sufficiently large compared with the cylinder diameter that we expect the theory does not accurately model the coupling between waves and the cylinder. The range of validity of the boundary layer approximation was studied in detail both numerically and analytically by Hurley & Keady (1997).

In reality, a viscous boundary encompasses the cylinder as it oscillates and the boundary layer approximation (i.e. $\partial/\partial r \ll \partial/\partial\sigma$) breaks down close to the cylinder surface. For small-amplitude oscillations ($A \ll R$) and neglecting the effects of density variations across the diameter of the cylinder, it can be shown that the boundary

thickness is (e.g. see Batchelor 1967, § 5.13)

$$\delta \simeq \sqrt{2\nu/\omega}, \tag{3.9}$$

which is independent of the amplitude and size of the cylinder. Close to points where the characteristics of waves tangentially contact the cylinder, Hurley & Keady (1997) showed that the motion within this small region is described by $\nabla^4\psi = 0$, and that this equation should hold for $r \ll R\sqrt{\lambda} = \sqrt{\nu/2\omega}\tan\Theta$. This is also of the same order of magnitude as the above estimate for the boundary layer thickness if the waves propagate at angles sufficiently far from the horizontal and vertical (i.e. $0^\circ \ll \Theta \ll 90^\circ$). For experiments presented here, $0.22\,\mathrm{s}^{-1} \leqslant \omega \leqslant 0.55\,\mathrm{s}^{-1}$, and $0.30\,\mathrm{cm} \geqslant \delta \geqslant 0.19\,\mathrm{cm}$. Thus we expect the boundary layer thickness to be approximately $10\% - 20\%$ the radius of the cylinder, and we anticipate discrepancies on this order between the theoretically predicted beam width and the experimentally determined width.

Because the upward and downward propagating internal wave beams are of relatively large amplitude where they intersect, we anticipate nonlinear effects due to wave–wave interactions may not be negligible. We evaluate the relative importance of these effects in the following section.

4. Results

A wide range of experiments have been performed in which we examine the structure of a beam of internal waves generated by an oscillating circular cylinder. We compare with theory the viscous decay of the beam, examining how the structure and amplitude of the waves vary with the amplitude and frequency of the cylinder motion.

4.1. *Basic-state fields*

Figure 3 shows the ΔN^2 (figure 3*a*) and $(N^2)_t$ (figure 3*b*) fields for a beam of internal waves propagating upwards and to the right of an oscillating cylinder. The fields are shown as the cylinder is moving downwards through its equilibrium position after six oscillations have been completed. Superimposed in white on both images are end views of the cylinder and its supporting rod. In this case, the cylinder oscillates at a frequency of $\omega = 0.46\,\mathrm{s}^{-1}$ with an amplitude $A \simeq 0.32\,\mathrm{cm}$, and the background stratification has buoyancy frequency $N \simeq 1.0 \pm 0.05\,\mathrm{s}^{-1}$. The $(N^2)_t$ field is calculated by comparing two images taken one second apart, this time difference being chosen as a value sufficiently small compared with the cylinder period (in this case 13.6 s) but not so small that noise dominates the signal. A comparison of figures 3(*a*) and 3(*b*) shows that the $(N^2)_t$ field leads the ΔN^2 field in phase by approximately $\pi/2$. As will be shown below, this behaviour is consistent with the transport of momentum upwards and to the right of the cylinder.

Linear theory predicts the internal wave beam propagates at an angle $\Theta = \cos^{-1}(\omega/N) \simeq 62.8^\circ$ to the vertical. This may be seen by comparison with the dashed lines superimposed on figure 3. The structure of the internal wave beams that propagate away from the cylinder in the other three quadrants can be inferred by symmetry, as discussed in the Appendix. Therein it is shown that ψ and $w = \partial\psi/\partial x$ exhibit even reflection symmetry about the x-axis, and $u = -\partial\psi/\partial z$, ΔN^2 and $(N^2)_t$ exhibit odd reflection symmetry about the x-axis.

The flow around the cylinder is observed to be laminar with a Reynolds number of $Re = 10$ based on the maximum velocity and displacement of the cylinder. The

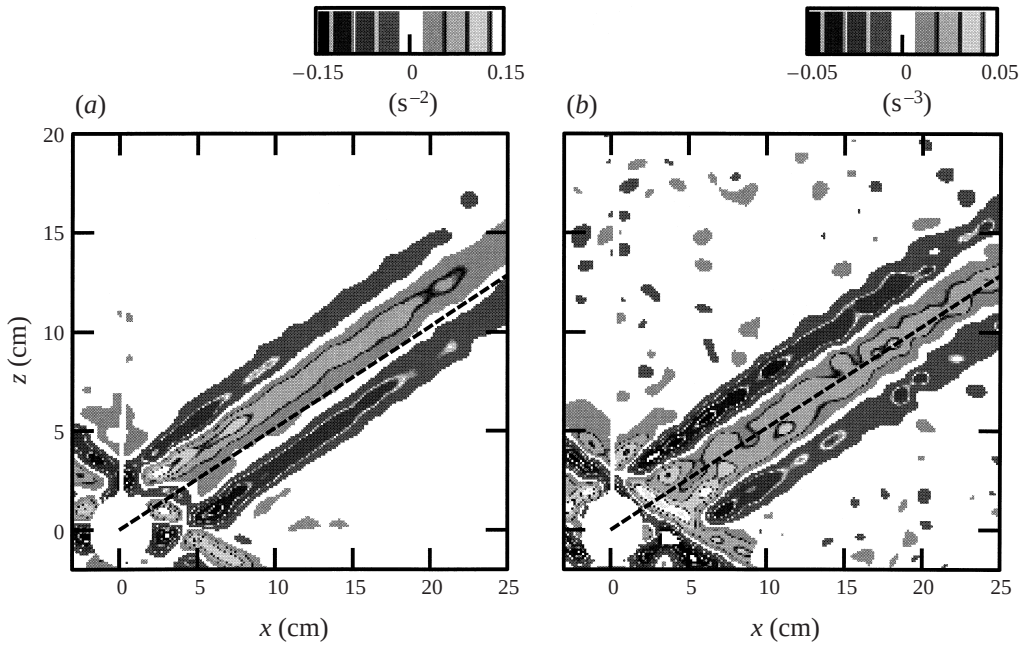

FIGURE 3. (*a*) ΔN^2 and (*b*) $(N^2)_t$ fields of internal waves generated by a vertically oscillating circular cylinder (superimposed in white) with centre initially at $x = z = 0$ cm. The barrier, inserted to block bottom reflections, is superimposed in white below $z = 0$ cm near $x = 10$ cm. The fields are shown for $-3 \leqslant x \leqslant 25$ cm and $-2 \leqslant z \leqslant 20$ cm with $|\Delta N^2| \leqslant 0.15\,\mathrm{s}^{-2}$ and $|(N^2)_t| \leqslant 0.05\,\mathrm{s}^{-3}$, and as the cylinder moves downward through its equilibrium position.

viscous scale for internal waves in this experiment is, from (1.3), $\ell_v \simeq 1.3R$. Because ℓ_v is comparable to the cylinder radius R, we might expect to see a bimodal structure close to the cylinder. Recall that where the beam is bimodal the envelope of the wave beam has maxima along lines approximately tangential to the cylinder at an angle Θ to the vertical. Where the beam is unimodal the envelope is largest along a line through the centre of the cylinder oriented at the same angle Θ. Figure 3 demonstrates the transition from a bimodal to a unimodal wave beam structure. In both diagrams of figure 3 the amplitude of the beams is largest close to the tangential lines within approximately 8 radii of the cylinder. Beyond this distance the peak amplitude occurs along a line through the centre of the cylinder. According to Makarov *et al.* (1990), the maximum distance from the cylinder centre over which the wave beam structure is expected to be bimodal is, from (1.4), $R_v \simeq 279R$. We see that this greatly over-predicts the observed transition distance.

The broadening of the beams where they are unimodal should, in theory, obey the $r^{1/3}$ power law found by Thomas & Stevenson (1972). However, the recorded along-beam extent of the viscously governed regime in these experiments is not sufficiently large to test this assertion.

By integrating the ΔN^2 and $(N^2)_t$ fields according to (2.12), (2.13), (2.14) and (2.15), the density, vertical displacement, and velocity fields are calculated assuming the average perturbation is zero over each cross-section. These fields, corresponding to the waves shown in figure 3, are shown in figure 4. In each diagram, the fields are shown between 2 and 25 cm to the right of the cylinder and between 2 and 20 cm above the cylinder. Figure 4(*a*) shows that the perturbations in the density field are

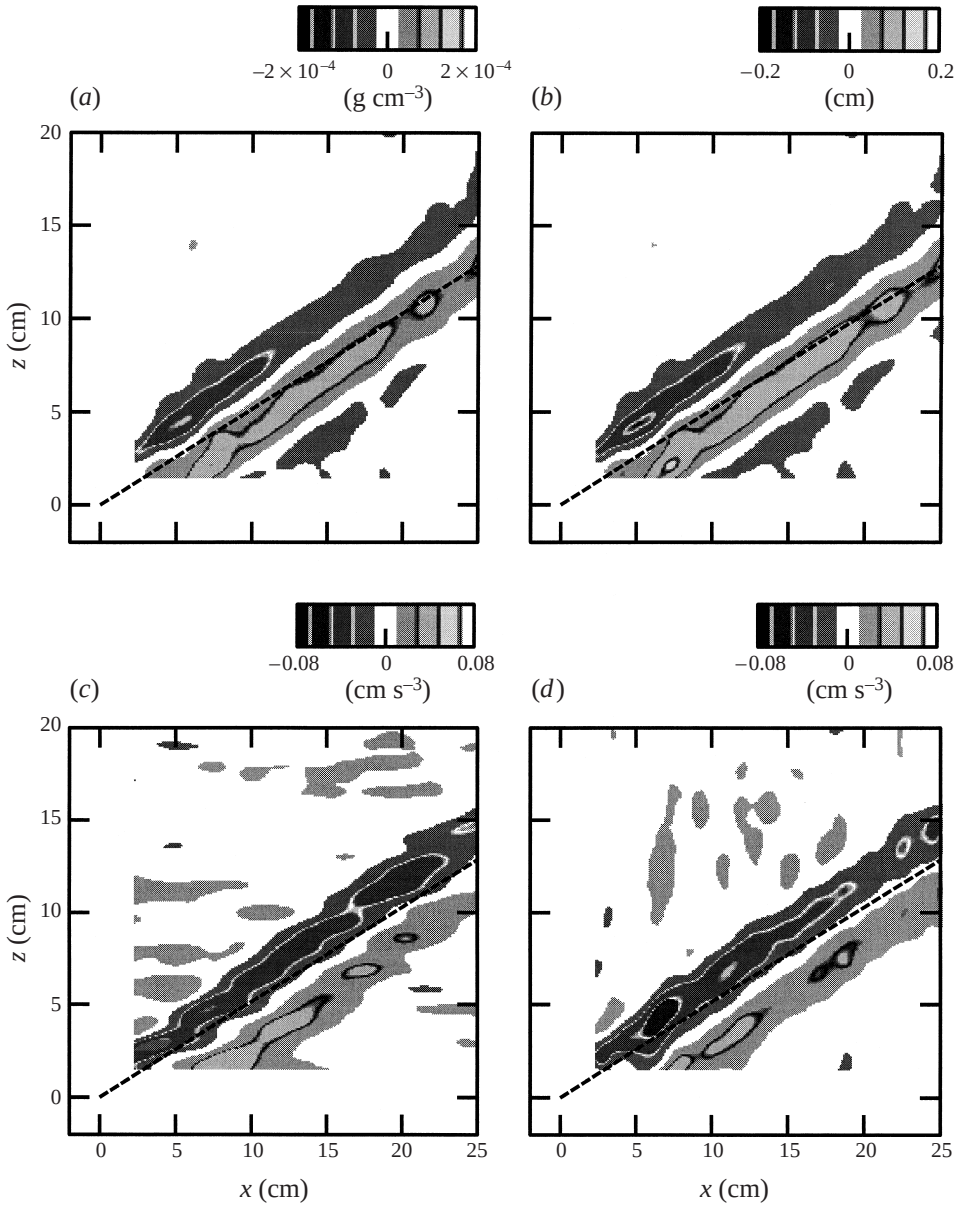

FIGURE 4. (*a*) Fluctuation density (ρ'), (*b*) vertical displacement (ζ'), (*c*) horizontal velocity (u'), and (*d*) vertical velocity (w') fields shown at the same time as in figure 3. All four fields are shown for $2 \leqslant x \leqslant 25$ cm and $2 \leqslant z \leqslant 20$ cm with $|\rho'| \leqslant 0.0002$ g cm^{-3}, $|\zeta'| \leqslant 0.2$ cm, and $|u'|, |w'| \leqslant 0.08$ cm s^{-1}.

of the order 10^{-4} g cm^{-3} for $r > 2R$. This corresponds to vertical displacements (see figure 4*b*) of approximately ± 0.1 cm, about 6% of the cylinder radius and about 30% of the amplitude of oscillation. The horizontal and vertical velocity fields are shown in figures 4(*c*) and 4(*d*), respectively, both scales ranging from -0.08 to 0.08 cm s^{-1}. The error associated with the measured velocity fields close to the cylinder ($r < 6R$) can be as large as 50%. This occurs because errors accumulate when integrating according to (2.14) and (2.15). Far from the cylinder the errors are less pronounced, and we estimate

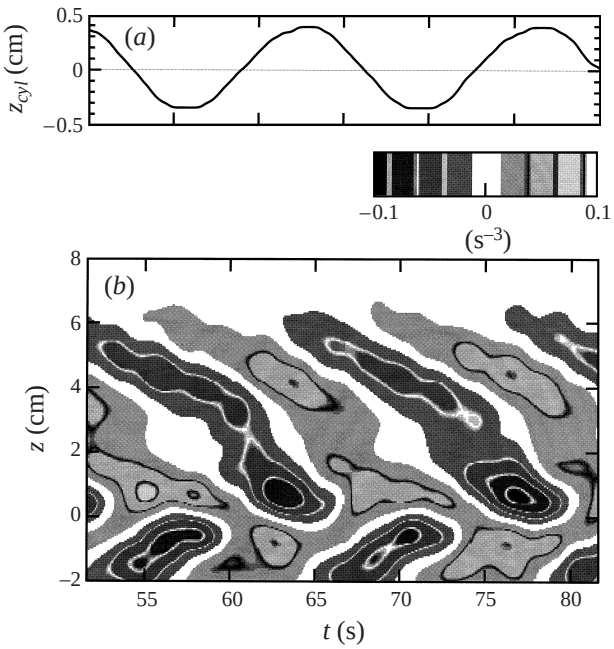

FIGURE 5. (*a*) Vertical displacement of cylinder, determined from video images, as it oscillates for 30 s, and over the same time (*b*) a space–time diagram of the $(N^2)_t$ field for a vertical cross-section 5 cm to the right of the cylinder extending from 2 cm below the centre of the cylinder to 8 cm above it. The curve does not appear to be a perfect sinusoid because its displacement is measured at coarse resolution from video: the true displacement is a smooth, continuous variation. Note that the fields shown in figures 3 and 4 occur at time $t = 81.6$ s.

them to be smaller than 20% for $r > 10R$. As expected, the velocity fields are out of phase with the perturbation density field by approximately a quarter-cycle, which is consistent with there being no net mass flux due to linear internal waves. Similarly, the two velocity fields are in phase, and the vertical flux of horizontal momentum $\rho_0 \langle u'w' \rangle$ is positive. By averaging the product of the horizontal and vertical velocity components across the width of the beam, we estimate its associated momentum flux per unit mass near $r \approx 10R$ to be approximately 0.0005 cm^2 s^{-2}. Therefore, the total of the magnitude of the flux from all four wave beams is approximately 0.002 cm^2 s^{-2}. Although beyond the scope of this paper, a more accurate measure of the momentum flux can be made by examining time-series of horizontal cross-sections of the flow (Sutherland & Linden 1998).

In addition to the spatial structure of the waves shown in figures 3 and 4, a space–time plot is constructed to show the evolution of the waves. Such a time series may be constructed by extracting a vertical cross-section from numerous video images, separated by intervals as short as 0.04 s. This method is particularly useful for determining the $(N^2)_t$ field, such as that in figure 3(*b*), since signal noise and thermal noise in the laboratory, which occur on a faster time scale than the waves, may be filtered efficiently.

Figure 5(*a*) shows the displacement of the cylinder from its equilibrium position between $t = 51.6$ and 81.6 s, as determined using video images of the same experiment from which the ΔN^2 and $(N^2)_t$ fields in figure 3 were calculated. (The fields in figure 3 are shown at time $t = 81.6$ s.) Figure 5(*b*) shows a space–time plot of the $(N^2)_t$ field for a vertical cross-section 5 cm to the right of the cylinder during the same period as

the plot in figure 5(*a*), and for a vertical section between −2 cm and +10 cm relative to the centre of the cylinder. The field, which is shown for values ranging from −0.1 to 0.1 s^{-3}, clearly illustrates that the overlapping waves have maximum amplitude near $z = \pm 1$ cm and that the waves along the right, upward propagating beam have maximum amplitude near $z = 4$ cm. The frequency of the waves is the same as that of the cylinder ($\omega = 0.46\,s^{-1}$), and the vertical phase speed, which is estimated from the slope of the phase lines at $z = 4$ cm, is approximately $c_{pz} \simeq -0.28\,cm\,s^{-1}$. This value may be used together with linear theory for plane internal waves to characterize the spatial structure of the wave field. Using $k_x = (\omega/c_{pz})\cot\Theta \simeq 0.84\,cm^{-1}$ and $k_z = \omega/c_{pz} \simeq 1.64\,cm^{-1}$, the horizontal and vertical wavelengths are approximately 7.4 cm and 3.8 cm, respectively, which is consistent with the structure of the waves shown in figure 3 near $x = 5$ cm and $z = 4$ cm.

The upward and downward propagating beams on either side of the cylinder are observed to overlap. If λ, defined by (3.5), and the wave amplitude are small then, as shown in the Appendix, the theory of Hurley & Keady (1997) predicts that the ΔN^2 and $(N^2)_t$ fields should vanish along the x-axis. However, figure 5(*b*) shows that $(N^2)_t$ is not identically zero where $z = 0$, but fluctuates periodically between positive and negative values. It is believed that this discrepancy occurs because in the experiments either the wave amplitude or $\lambda \simeq 0.002$ is not sufficiently small for the theory to hold. It seems likely that large-amplitude effects are primarily responsible because the fluctuations are larger closer to the cylinder, and we have observed that the fluctuations increase with increasing amplitude of oscillation. Interestingly, the fundamental period of the fluctuations at $z = 0$ is half the cylinder oscillation period. Indeed, if the oscillation period is sufficiently long ($\omega < N/2$), this region can act as a source of internal waves with a frequency double that of the cylinder frequency. The frequency-doubling excitation, which preliminary study suggests may occur due in part to nonlinear wave–wave interactions, is currently under investigation.

4.2. *Effect of forcing amplitude*

By suspending the cylinder at different positions along the oscillating arm, the amplitude of the oscillating cylinder is varied, allowing us to examine how the amplitude and structure of the internal waves varies with the forcing amplitude.

Figure 6 shows the ΔN^2 field from the same experiment examined in figures 3, 4, and 5: the amplitude is 0.32 cm, the cylinder oscillates with frequency 0.46 s^{-1}, and the background buoyancy frequency is $N \simeq 1.0\,s^{-1}$. Here, the waves are shown at four different times during one period of oscillation: $T/2$ (as the cylinder moves upward through its equilibrium position), $5T/8$, $3T/4$, and $7T/8$. Each field is shown over a $15 \times 15\,cm^2$ region, with the cylinder in its equilibrium position at the origin. The scale is the same in each diagram with $|\Delta N^2| \leqslant 0.18\,s^{-2}$. The successive fields show the downward propagation of phase lines in time, as expected for internal waves that propagate energy upward.

Figure 7 shows the ΔN^2 field for a beam of internal waves generated by a cylinder oscillating with amplitude 0.213 cm, two-thirds the amplitude used to generate the waves shown in figure 6. The frequency of oscillation is the same as before and each diagram shows the field corresponding to the same approximate phase of oscillation as in figure 6. The scale for ΔN^2 has been adjusted by a factor of two-thirds to match the relative forcing amplitude of the case with $A = 0.32$ cm. Thus, if changing the cylinder amplitude results in a linear change in the internal wave amplitude, the corresponding diagrams of both figures would be appear to be approximately the

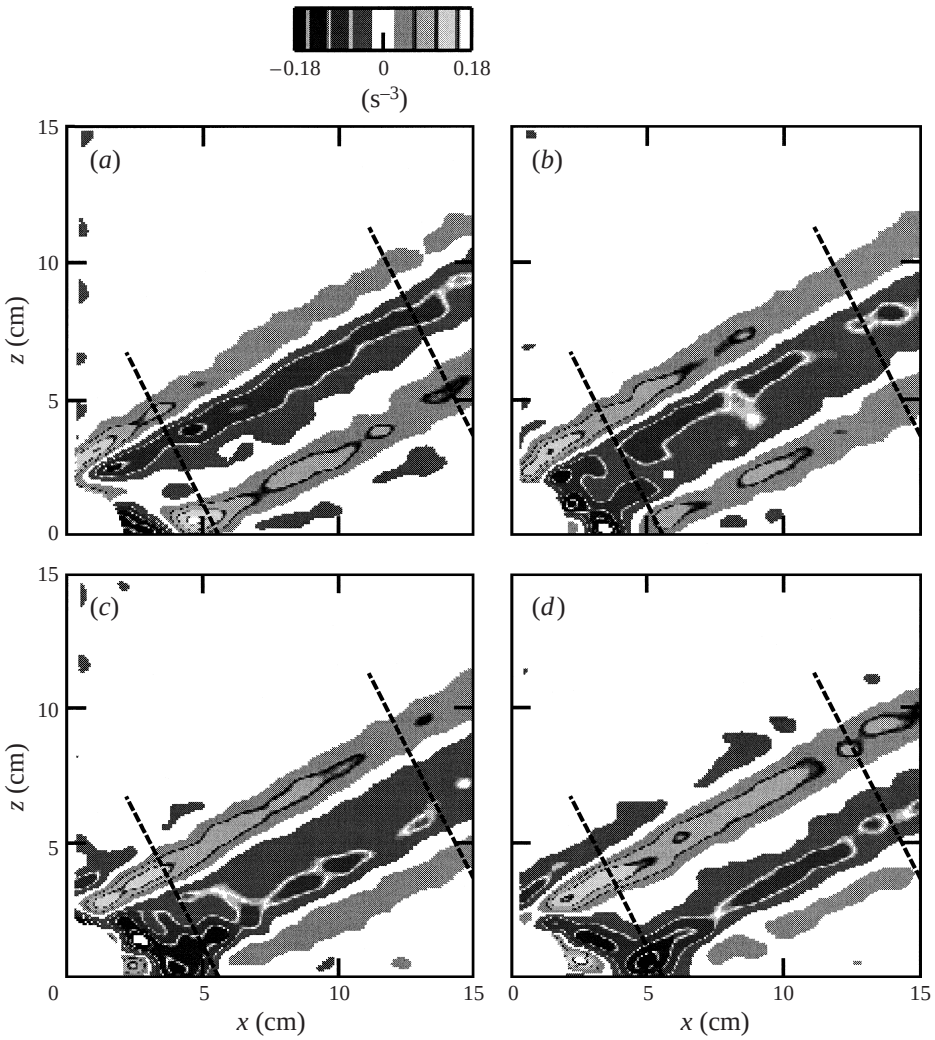

FIGURE 6. The structure of internal waves generated by a cylinder (shown superimposed in white) oscillating vertically with large amplitude ($A = 0.32$ cm) at four times during one period (T): (*a*) $T/2$, (*b*) $5T/8$, (*c*) $3T/4$, and (*d*) $7T/8$. The first of these corresponds to the cylinder moving upward through its equilibrium position. All four fields are shown for $0 \leqslant x \leqslant 15$ and $0 \leqslant z \leqslant 15$. The superimposed diagonal dashes indicate where cross-sections are taken for the plots shown in figures 8 and 9.

same. In general, however, the normalized wave amplitudes are moderately larger (by approximately 5%) for smaller amplitude forcing.

We compare with theory the waves generated by the two forcing amplitudes by looking at across-beam sections 3 and 9 radii from the cylinder. The positions of these cross-sections are shown by the superimposed dashed lines on each diagram of figures 6 and 7. Considering that no calibration or adjustment of data beyond noise filtering has been performed, the agreement between experiment and theory is, in general, remarkably good.

The cross-sections taken at a distance $r = 3R$ from the cylinder are shown in figure 8 with each diagram corresponding respectively to the same phase of oscillation as

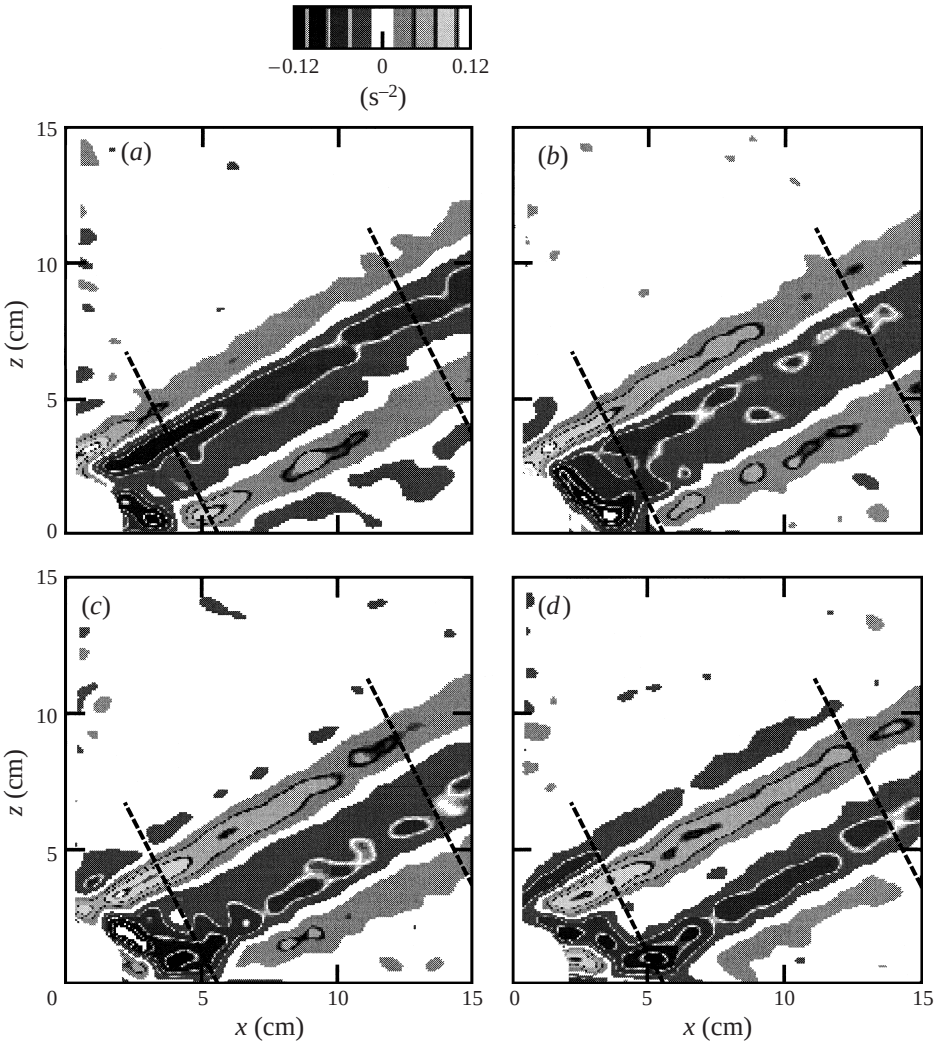

FIGURE 7. As in figure 6, but for a smaller oscillation amplitude ($A = 0.213$ cm).

in figures 6 and 7. As in § 3, the coordinate σ is perpendicular to the beam, with $\sigma = 0$ corresponding to the centre of the beam and oriented such that σ increases in a direction upward and to the left. In both figures ΔN^2 is normalized by the cylinder amplitude A. The solid line shows the prediction using the Hurley & Keady (1997) theory, the long-dashed line shows values from experiments for the larger amplitude oscillations ($A = 0.32$ cm) while the short-dashed line shows values for the smaller amplitude oscillations ($A = 0.213$ cm). The theoretical solution is calculated for the superposition of the right, upward and downward propagating wave beams. The theory agrees well for $\sigma > -R$. The greatest discrepancies occur in the region where the two beams overlap ($\sigma < -R$). In part, this is the result of weakly nonlinear effects, which are not captured by linear theory.

In each diagram of figures 6 and 7 the phase is slightly different between the experiments and theory due to the manual synchronization used to grab frames from video: the exact time at which the frame is acquired can differ from the desired time

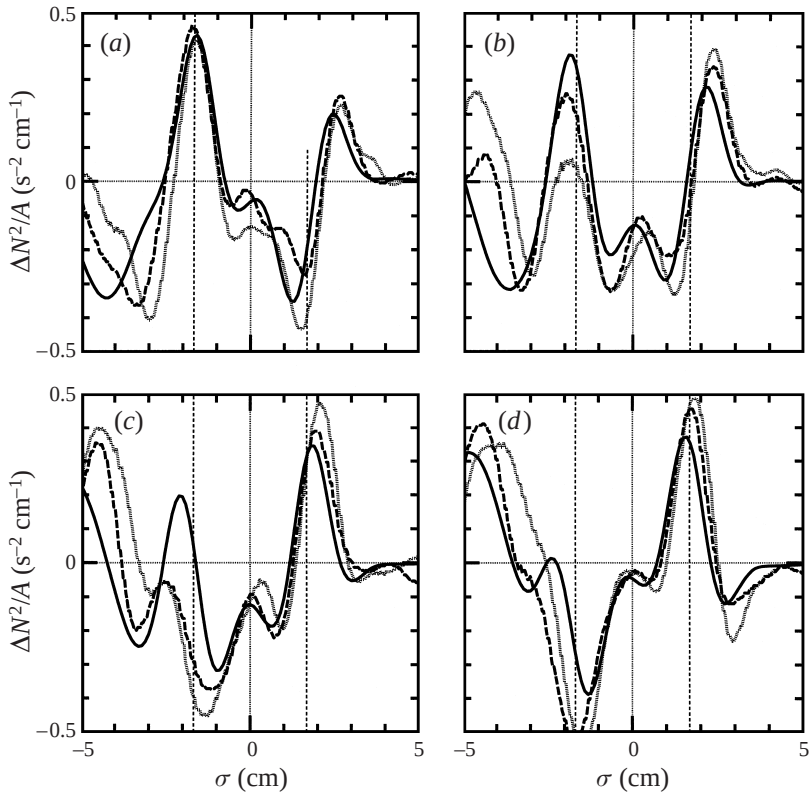

FIGURE 8. Comparison of non-dimensional amplitude $\Delta N^2/A$ of internal waves between theory (solid line) and experiment for a cylinder oscillating vertically at large amplitude ($A = 0.32$ cm; long-dashed line) and smaller amplitude ($A = 0.213$ cm; short-dashed line) along a cross-section $-5 \leqslant \sigma \leqslant 5$ perpendicular to the beam 3 cylinder radii (5.03 cm) from the cylinder centre. Large values of σ correspond to the position on the upper flank of the upward and rightward propagating beam of internal waves. The diagrams show $\Delta N^2/A$ at four times during one period (T): (*a*) $T/2$, (*b*) $5T/8$, (*c*) $3T/4$, and (*d*) $7T/8$. The vertical dashed lines indicate the extent of the cylinder diameter. The full spatial structure of the ΔN^2 fields at each time is shown in figures 6 and 7, where the superimposed diagonal lines closest to the cylinder correspond to the cross-sections taken in the current figure.

by up to 0.5 s. For these experiments, therefore, the error in the phase shift can be as large as 5%. Nonetheless, the plots for large- and small-amplitude forcing exhibit the same structure for the four phase angles shown. As expected for upward propagating internal waves (with negative vertical phase speed), the phase lines shift to smaller values of σ as time advances. As well as the coordinate axes, the vertical dashed lines on each diagram indicate where tangents to the cylinder (in its equilibrium position) parallel to the beam intersect the cross-section. These indicate that the separation between the two largest peaks of the wave amplitude is somewhat larger than the separation of the two tangents and that this separation is larger for smaller amplitude waves.

The theory consistently under-predicts the experimentally measured amplitude and width of the wave beams. The width is under-predicted because the theory neglects the development of a viscous boundary layer surrounding the cylinder. According to (3.9), the width of this layer is expected to be on the order of $\delta \simeq 0.2$ cm in approximate agreement with the observed discrepancy between theory

and experiment. Although the predicted boundary layer thickness is independent of oscillation amplitude, experiments show that the width of the beam is larger (by approximately 5%) for experiments with $A = 0.21$ cm compared with those with $A = 0.32$ cm. The theory used to derive (3.9) is independent of the amplitude of oscillation of the cylinder because it assumes that A is small compared with δ, which is not the case here. Therefore, a second-order correction to (3.9) is required. Neglecting the effects of density variations over the extent of the cylinder, we estimate the correction is the result of a steady streaming motion in the form of a standing wave within the boundary layer surrounding the cylinder (e.g. Batchelor 1967, § 5.13). The boundary layer fluctuates in thickness by approximately $\delta_2(A) = (3/2)A^2/R$ about nodal points of the flow, which is a function of the oscillation amplitude A. Thus $|\delta_2(0.32) - \delta_2(0.213)| \simeq 0.05$ cm represents the expected difference in boundary layer thickness for the two amplitudes considered here. Nonetheless, it is not understood why the boundary layer width is smaller for larger amplitude forcing.

The effect of the change in boundary layer thickness upon the normalized wave amplitude can be seen in figure 8. Despite the experimental noise in the ΔN^2 fields, which leads to some spurious fluctuations, the plots show consistent differences between cases with large- and small-amplitude forcing. When normalized by the forcing amplitude A, the peak values of $\Delta N^2/A$ on the lower flank of the beam are generally smaller for larger A because larger shear is generated which leads to enhanced viscous dissipation. In addition, the difference between large- and small-amplitude forcing on the motion in the lower flank of the beam increases due to the interference between the upward and downward propagating beams that emanate from the cylinder. Where the two beams cross, two weakly nonlinear effects may occur. First, large-amplitude structures on small scales may dissipate viscously at a more rapid rate than predicted by linear theory. Second, if the waves are of sufficiently low frequency ($\omega < N/2$) then, as discussed earlier, additional energy can be radiated away from the overlapping region by waves of double the frequency of the primary wave beams.

Further from the cylinder the asymmetric behaviour is less pronounced because the wave beams widen due to viscous attenuation and the maximum amplitude is reached along a line through the cylinder centre rather than at the tangents. This is evident in figure 9 where plots of $\Delta N^2/A$ along cross-sections 9 radii from the cylinder centre are compared for large- and small-amplitude forcing. However, at this distance from the cylinder centre the amplitude envelope is broader and the peaks themselves not as large. This makes differences between the $\Delta N^2/A$ profiles for large- and small-amplitude forcing more difficult to distinguish over the signal noise.

4.3. *Effect of forcing frequency*

A series of experiments were conducted to determine how the structure of the internal wave beams varies with the forcing frequency ω. For comparison with the results in figures 3 to 6, the buoyancy frequency and oscillation amplitude were maintained at the same values, $N \simeq 1\,\mathrm{s}^{-1}$ and $A = 0.32$ cm, respectively.

Figure 10 shows the ΔN^2 field with the internal wave beam in a coordinate system (r, σ). Note that a spatially anisotropic scaling of these images has been used to emphasize the structure of the flow. Because N^2 varies by $\pm 5\%$ with height, the beam tilts slightly upward in the (r, σ) coordinate system which has been rotated from the (x, z) coordinate system by an angle $\Theta = \cos^{-1}(\omega/N)$. Four experiments are shown with forcing frequencies of $\omega = 0.26$, 0.36, 0.46 and $0.55\,\mathrm{rad\,s}^{-1}$ in figures 10(a) to 10(d), respectively. Taking $N = 1\,\mathrm{s}^{-1}$ exactly, internal wave beams are generated at angles

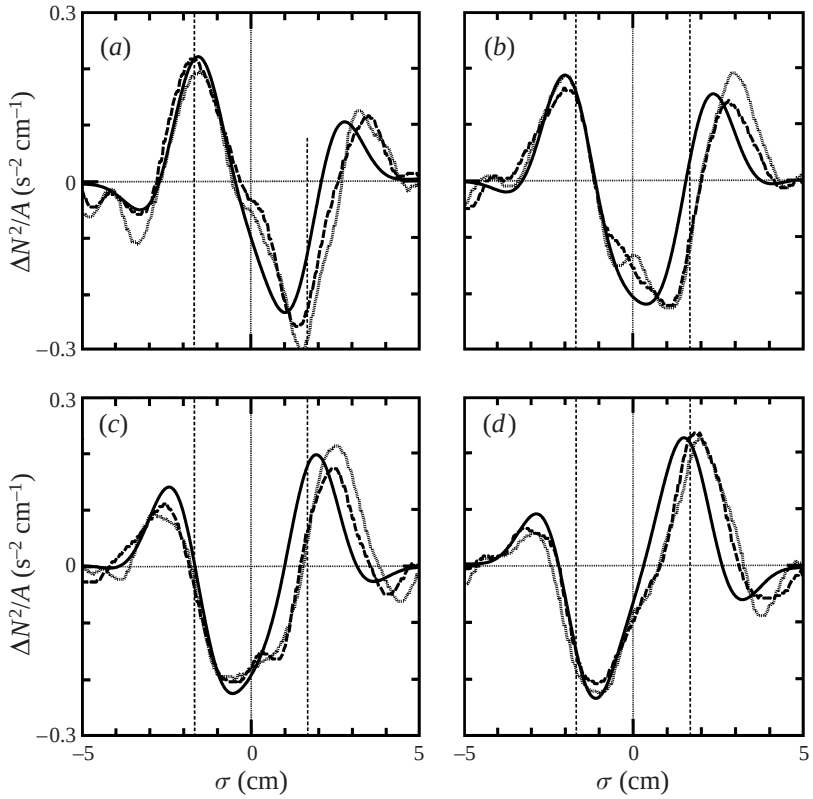

FIGURE 9. As in figure 8, but for cross-sections taken perpendicular to the beam 9 cylinder radii (15.08 cm) from the cylinder centre. The full spatial structure of the ΔN^2 fields at each time is shown in figures 6 and 7, with the cross section taken along the further diagonal line to the cylinder superimposed the figures.

to the vertical Θ of 74.9°, 69.9°, 62.8° and 56.9°, respectively. Each field is shown for $0 \leqslant r \leqslant 20$ cm and $-5 \leqslant \sigma \leqslant 5$ cm. The phase of oscillation of the cylinder is approximately the same in all four cases. Experiments were performed with larger forcing frequencies, but waves reflected from the bottom of the tank interfered with the primary beam. For clarity those results are not presented here.

We observe that the shallower wave beams (i.e. Θ large) are of moderately smaller amplitude. The normalized peak-to-peak amplitude is approximately 15% smaller for $\Theta = 76.9°$ than for $\Theta = 56.9°$. This behaviour is anticipated because energy is transported away from the source more efficiently by horizontally oriented waves, and therefore, the energy density close to the source is expected to be smaller. From linear theory, the magnitude of the group velocity of inviscid, monochromatic internal waves is

$$|\boldsymbol{c}_g| = \frac{Nk_x}{k_x^2 + k_z^2} = \frac{N}{k_\sigma} \sin\Theta, \tag{4.1}$$

in which k_x, k_z and k_σ are the horizontal, vertical and across-beam wavenumbers, respectively. For waves generated by a cylinder of radius R, the dominant across-beam wavenumber k_σ is approximately independent of ω, and therefore the magnitude of the group velocity is largest when $\Theta = 90°$.

Corresponding to the diagrams of figure 10, figure 11 plots across-beam cross-

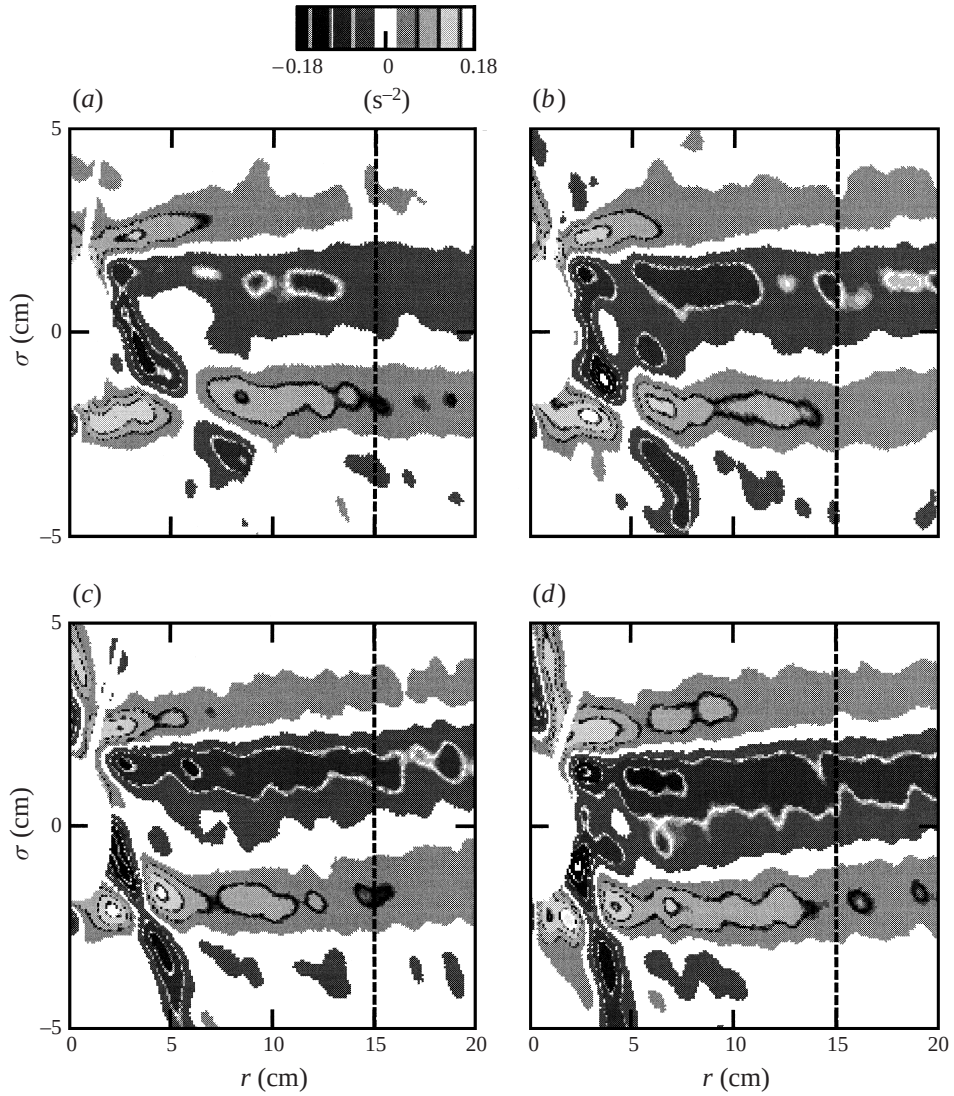

FIGURE 10. The structure of internal waves generated by a cylinder (shown superimposed in white) oscillating vertically with large amplitude ($A = 0.32$ cm) at four oscillation frequencies corresponding to internal wave beams propagating at an angle to the vertical of (*a*) 74.9°, (*b*) 69.9°, (*c*) 62.8°, and (*d*) 56.9°. The barrier, inserted in the tank to block bottom reflections, is apparent in diagram (*a*) near $\sigma = -3$ cm, $r = 10$ cm. The waves are each shown at the same phase, when the cylinder moves downward through its equilibrium position. All four fields are shown in a rotated frame of reference with $0 \leqslant r \leqslant 20$ cm in the along-beam direction and $-5 \leqslant \sigma \leqslant 5$ cm in the cross-beam direction such that positive σ corresponds to the upper side of the beam. The superimposed vertical dashes indicate where cross-sections are taken for the plot shown in figure 11.

sections of $\Delta N^2/A$ at a distance $r = 9R$ from the centre of the cylinder. The positions of these cross-sections are shown by the dashed lines superimposed on each diagram of figure 10.

The structure of the waves is approximately the same in all four cases, although the amplitude is somewhat smaller for shallower wave beams. However, the Hurley &

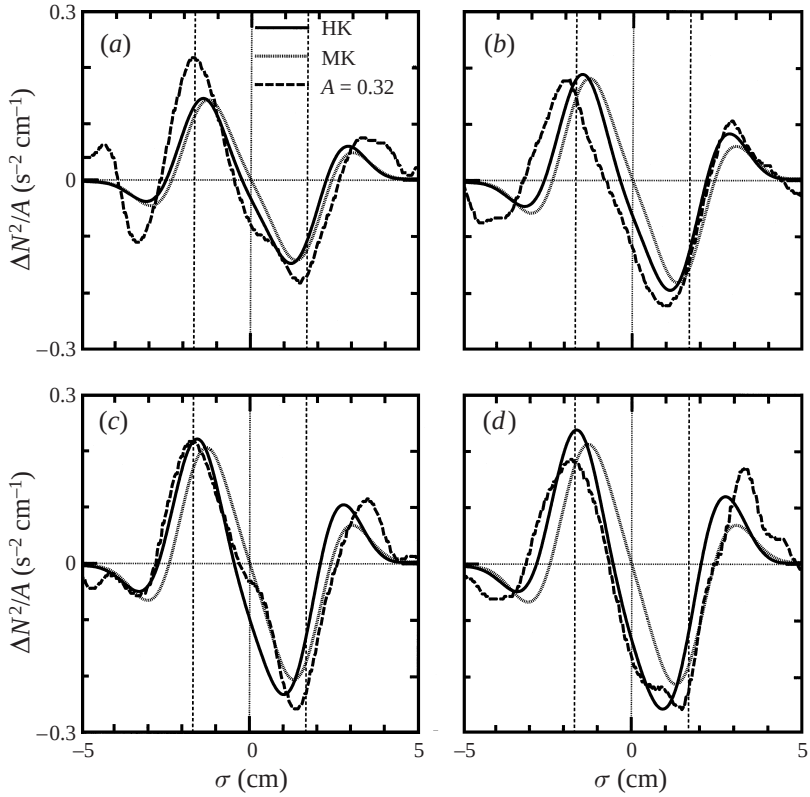

FIGURE 11. Comparison with Hurley & Keady (1997) theory (solid line), Makarov *et al.* (1990) theory (dotted line) and experiment (dashed line) of $\Delta N^2/A$ of internal waves generated by a cylinder oscillating vertically at large amplitude ($A = 0.32$ cm) for the cylinder oscillating at four frequencies corresponding to a wave beam propagating (*a*) 74.9°, (*b*) 69.9°, (*c*) 62.8°, and (*d*) 56.9° along a cross-section $-5 \leqslant \sigma \leqslant 5$ perpendicular to the beam 9 cylinder radii (15.08 cm) from the cylinder centre. Large values of σ correspond to the position on the upper flank of the upward and rightward propagating beam of internal waves. The vertical dashed lines on each diagram indicate the extent of the cylinder diameter. The full spatial structure of the ΔN^2 field at each oscillation frequency is shown in figure 10.

Keady (1997) theory (indicated by solid lines) significantly under-predicts the peak-to-peak amplitude of shallow beams (e.g. by 25% for $\Theta = 74.9°$), and moderately over-predicts the peak-to-peak amplitude of higher frequency waves (e.g. by 10% for $\Theta = 56.9°$).

We also compare the experimental results with the theoretical predictions made by Makarov *et al.* (1990). For the vertically oscillating cylinder, their solution differs moderately from that of Hurley & Keady (1997) in amplitude and phase, with the factor $\exp(\mathrm{i}\Theta)$ before the integral in (3.6) being replaced by $\mathrm{i}\sin(\Theta)$. As pointed out by Hurley (1997) and Hurley & Keady (1997), although the Makarov *et al.* result is a solution of (3.4), in the limit of zero viscosity it does not correspond with the exact inviscid solution given by Appleby & Crighton (1986), and the solution is therefore unsatisfactory. The theoretical solutions by Makarov *et al.* (1990) are shown by the dotted lines in figure 11. In all four diagrams, these solutions are found to agree less well with experimental results than the solutions by Hurley & Keady (1997). As

	Theory		Experiment		Ratio of Theor./Exp.	
Θ (deg.)	Width	Amplitude	Width	Amplitude	Width	Amplitude
74.9	1.29	0.41	1.51	0.56	0.85	0.73
69.9	1.30	0.54	1.47	0.56	0.88	0.96
62.8	1.30	0.63	1.57	0.66	0.83	0.96
56.9	1.31	0.69	1.52	0.62	0.86	1.12

TABLE 1. Theoretically predicted normalized wave beam widths and amplitudes of the ΔN^2 field are compared with those determined from experiments of internal waves generated by a cylinder oscillating with amplitude $A = 0.32$ at four different frequencies, each beam forming an angle Θ with the vertical. Widths are normalized by the cylinder radius $R = 1.67$ cm and the amplitudes are normalized by AN^2/R^2. The corresponding predicted and observed across-beam structures of the waves determined 9 cylinder radii from the source are shown in figure 11.

expected, although the difference in amplitude between the two theoretical solutions is small in each case, the phase difference is larger for shallower waves.

In table 1 we compare quantitatively the normalized beam width and amplitude of the ΔN^2 field with the values predicted theoretically by Hurley & Keady (1997). The non-dimensional beam width for both theory and experiment is estimated as $\Delta/2R$ in which Δ is the distance between the largest positive peaks on each flank of the beam. The normalized amplitude is estimated to be half the difference between the maximum and minimum value of $\Delta N^2/(AN^2/R^2)$. The table shows that the theoretically predicted beam width is consistently smaller than experiments by approximately 15%. This discrepancy is consistent with the scaling estimate for the cylinder boundary layer thickness given by (3.9). The theoretically determined amplitude under-predicts experimental values if the cylinder oscillates slowly and the wave beams are shallow. For waves that propagate more vertically, however, theory over-predicts the experimental results.

4.4. *Effect of nonlinear wave–wave interactions*

We also expect there to be enhanced attenuation of shallow waves due to nonlinear wave–wave interactions because the upward and downward propagating beams are superimposed over a larger area. To highlight the asymmetry between the upper and lower flank of one of the four internal wave beams, a time series of vertical cross-sections from the ΔN^2 field is constructed over two periods of the cylinder motion for large-amplitude oscillations at different frequencies. From these, a vertical profile of the root-mean-square amplitude of $(N^2)_t$ is calculated. By repeatedly performing this calculation for a series of horizontally spaced vertical cross-sections, it is possible to construct the r.m.s. amplitude of the wave beam everywhere in space. Figure 12 shows the results of this calculation for two experiments in which a cylinder oscillates at a low frequency of $0.26\,\mathrm{s}^{-1}$ and at a higher frequency of $0.55\,\mathrm{s}^{-1}$. The background buoyancy frequency in both cases is $N \simeq 1.0\,\mathrm{s}^{-1}$. In the sequence of vertical profiles of r.m.s. amplitude shown in figure 12(*a*) for the low-frequency case, the decay of the primary wave beam from a double-peaked structure to a broad single-peaked structure is apparent. Also visible in these plots is a smaller amplitude secondary wave beam oriented closer to the vertical. This beam is composed of waves that evolve with double the frequency of the primary wave beam. As such, the secondary wave beam can exist only if the frequency of the primary wave beam is less than $N/2$.

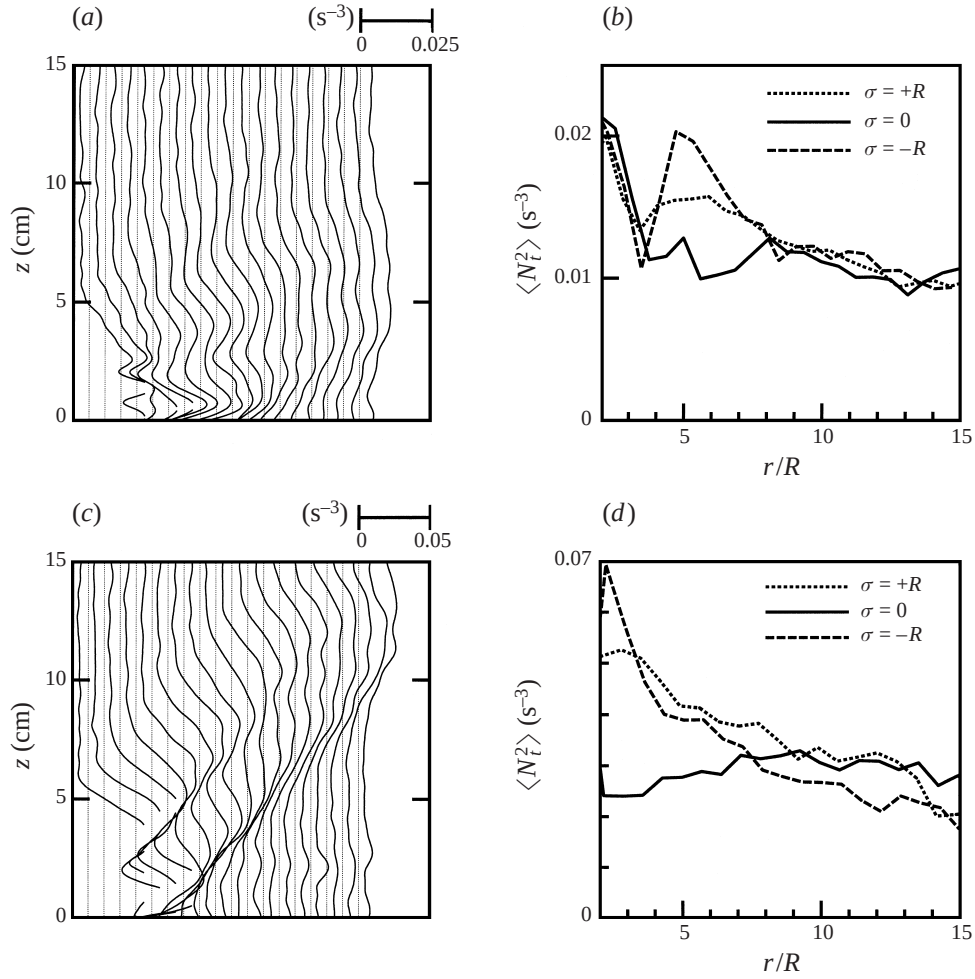

FIGURE 12. (*a*) 19 vertical profiles of the root-mean-square time averages of $(N^2)_t$, for a cylinder oscillating with frequency 0.26 rad s^{-1}, taken 2, 3,..., 20 cm horizontally from the cylinder centre (each profile is shifted horizontally and shown ranging from 0 to 0.025 s^{-3}. The missing segments in the profiles correspond to values of $(N^2)_t > 0.025\,\mathrm{s}^{-3}$ which could not be resolved. (*b*) Plots of these averages along sections at an angle $\Theta = \cos^{-1}(\omega/N)$ with the vertical and passing through the cylinder centre (solid line), tangential to the lower side of the cylinder (long-dashed line), and tangential to the upper side of the cylinder (short-dashed line). (*c*), (*d*), as (*a*) and (*b*), respectively, but for a cylinder oscillating with frequency 0.55 rad s^{-1}. The missing segments in the profiles for (*c*) correspond to values of $(N^2)_t > 0.05\,\mathrm{s}^{-3}$.

Analysis of the power spectrum of the time evolution of the cylinder displacement (not shown) indicates that the cylinder moves almost sinusoidally and that the secondary wave beam is not excited by the first harmonic of this motion. It is possible that the secondary wave beam is excited by a harmonic response of the stratified fluid to the oscillating source, such as that studied by Bell (1975). However, preliminary work suggests that the amplitude of the secondary wave beam increases approximately as the square of the amplitude of the primary wave beam. Furthermore, examination shows that the interference of the upward and downward propagating wave beam along the horizontal x-axis is not perfectly destructive, as predicted by

the linear theory of Hurley & Keady (1997). Indeed, as shown for example by figure 5, the waves interfere along the x-axis in a way that creates a disturbance of twice the frequency of the source. These observations lead us to believe that the secondary beam results, at least in part, from nonlinear wave–wave interactions of the upward and downward propagating wave beams. A detailed examination of this phenomenon is currently in progress. Figure 12(*b*) shows values of the r.m.s. amplitude along a radial line through the centre of the cylinder (solid line), tangential to the top of the cylinder (small-dashed line) and tangential to the bottom of the cylinder (large-dashed line), the three lines being oriented parallel to the beam at an angle Θ to the vertical. The plots show that the amplitude in the lower flank of the beam is larger than in the upper flank between 4 and 7 cylinder radii from the cylinder centre, where the upward and downward propagating beams overlap. Beyond this, the beam has approximately the same amplitude for $-R < \sigma < R$ up to 15 cylinder radii away. The single-peaked structure develops approximately 8 cylinder radii away from the cylinder.

Figure 12(*c*) is similar to figure 12(*a*) but is shown for an experiment with a cylinder oscillating at a higher frequency of $0.55\,\mathrm{rad\,s^{-1}}$. In comparison, the amplitude of the waves is much larger (the curves being shown on a scale from 0 to $0.05\,\mathrm{s^{-3}}$) and the transition from a double-peaked to a single-peaked structure is more pronounced. The plots of the amplitude along radial and tangential lines shown in figures 12(*d*) and 12(*b*) illustrate that motion in the lower flank is of large amplitude in the overlapping region, but further from the cylinder, motion in the upper flank is of larger amplitude. As in the low-frequency case, the single-peaked structure develops approximately 8 cylinder radii away from the cylinder, but in this case is more pronounced.

5. Conclusions

We have presented details of a new technique that we call 'synthetic schlieren', in which the amplitude of nominally two-dimensional internal gravity waves can be quantitatively and non-intrusively measured. The technique has been applied to the classical experiment in which internal gravity waves are generated by a vertically oscillating circular cylinder, focusing in particular on how the amplitude and structure of the waves are affected by different amplitudes and frequencies of forcing.

The overall agreement between theory and experiments was very good as is demonstrated by figure 11 which compares theoretical and experimental cross-sections of a wave beam at a distance $9R$ from the cylinder. The close agreement demonstrated that the synthetic schlieren technique is capable of making accurate measurements and also lends support to the theories.

However, in the experiment the displacement thickness of the oscillatory boundary layer that surrounds the cylinder is not negligible compared to the radius of the cylinder (as is assumed in the theory) so that the theoretically predicted beam widths are smaller than those observed. Effectively, the viscous boundary layers surrounding the cylinder act to increase the size of the source.

In general, we observe that the amplitude of the waves is proportional to the amplitude of the forcing. However, the relative amplitude is moderately smaller if the cylinder oscillates at larger amplitude. This occurs because the viscous boundary layer surrounding the cylinder is thinner and, therefore, relatively more energy is dissipated near the source.

For the typical parameters of our experiments, current theories predict unphysically large tangential velocities within half a cylinder radius of the source. This is a consequence of the 'boundary layer approximation' used to simplify the equations of

motion into a form with analytic solutions, but which neglects some aspects of the coupling between waves and the source. Experiments show that the Hurley & Keady (1997) theory under-predicts the amplitude of the smaller frequency (shallower) waves by as much as 15% at a distance $9R$ from the source.

Where the upward and downward wave beams overlap the agreement between theory and experiment is not so close. The theory predicts that $(N^2)_t$ is odd about the x-axis and, in particular, should vanish on the axis itself. However, the experimental value of $(N^2)_t$ on the x-axis, shown in figure 5, fluctuates non-negligibly between positive and negative values. The effect is most pronounced for large-amplitude forcing and, therefore, it is believed that the fluctuations occur because the waves generated in this case are of too large an amplitude for the theory to apply.

The transverse structure of the wave beam is generally well predicted by linear theory. However, whereas the envelope of the beam is predicted to be symmetric about its axis, we observe that it is asymmetric. This discrepancy is due to the interaction close to the cylinder of the two wave beams that propagate upward and downward from the cylinder. As a result, enhanced viscous dissipation and nonlinear wave–wave interactions locally attenuate motion in the flank of the beam where it crosses the horizontal axis. At smaller forcing frequencies when the horizontal extent of the interaction region is larger, the overall attenuation is in fact less. This is because the wave motion is of smaller amplitude and the nonlinear interaction is weaker.

In future work we will examine the effect that a different source shape and excitation motion has on the wave field. The wave field will be examined using a related optical method in which the displacement of a random array of dots is determined through pattern matching and the density gradient field is calculated accordingly. This method has the advantage of measuring horizontal as well as vertical fluid displacements due to the passage of internal waves.

If the flow is not two-dimensional, synthetic schlieren can yield useful qualitative information about the flow structure without the use of dyes or particles. If the flow is nominally two-dimensional across the span of the tank, quantitative measurements may be made. In particular, the technique should prove to be a powerful new tool with which to measure the momentum and energy flux of spanwise uniform internal waves. For example, synthetic schlieren has been successfully employed in a study by Sutherland & Linden (1998) to measure the momentum extracted by internal waves from a sheared mixing region in the wake of flow over a thin barrier. It is hoped that the method should prove equally useful in measuring the impact of an internal wave field incident upon and reflecting from a turbulent patch.

The authors would like to thank B. Voisin and G. Keady for useful discussions concerning the linear theory of internal waves generated by vibrating bodies. The authors would also like to thank one of the anonymous reviewers for comments which helped to illustrate better the comparisons between theory and experiment. This work has been supported in part by NERC under grant number GR3/09399.

Appendix. Symmetry and superposition of wave beams

Here we demonstrate the symmetry between the four wave beams emanating from a vertically oscillating cylinder, and we examine analytically the superposition of the upward and downward propagating wave beams in order to demonstrate that the ΔN^2 and $(N^2)_t$ fields interfere destructively along the horizontal axis through the cylinder centre.

First, we show that the streamfunction of the upward and downward propagating wave beams to the right of the cylinder exhibits a reflection symmetry across the x-axis.

The equation for the streamfunction of the right and upward propagating wave beam is given by (3.6). For the discussion below, this streamfunction is denoted by ψ_{R+}. The streamfunction of the right and downward propagating wave beam is denoted by ψ_{R-}. Similarly the streamfunctions of the left, upward and downward propagating wave beams are denoted by ψ_{L+} and ψ_{L-}, respectively.

Explicit formulae for each of these four streamfunctions are given by Hurley & Keady (1997). In particular, the rightward propagating beams are given explicitly by

$$\psi_{R\pm}(r,\sigma) = -\frac{iWR}{2}e^{i\Theta}\int_0^\infty \frac{J_1(K)}{K}\exp\left(-K^3\lambda\frac{r}{R} \mp iK\frac{\sigma}{R}\right)\,dK, \tag{A 1}$$

where $r > 0$ and σ are the along-beam and across-beam coordinates, respectively, oriented so that r increases with distance from the cylinder and positive values of σ correspond to the upper flank of each wave beam. (Note that Hurley & Keady (1997) used along-beam and across-beam coordinates $(s_\pm, \sigma_\pm)$ defined with an orientation different to that used here.) The angle Θ is measured clockwise from the vertical.

The formulae for the leftward propagating beams were also found by Hurley & Keady (1997), and may be simply expressed in terms of the rightward propagating beams from the relations

$$\psi_{L\pm}(r,\sigma) = -\psi_{R\mp}(r,-\sigma). \tag{A 2}$$

To compare the symmetry of the wave beams in a fixed, Cartesian (x,z) coordinate system, we note that for the upward propagating beams

$$(r,\sigma) = (x\sin\Theta + z\cos\Theta, -x\cos\Theta + z\sin\Theta), \tag{A 3}$$

and for the downward propagating beams

$$(r,\sigma) = (x\sin\Theta - z\cos\Theta, x\cos\Theta + z\sin\Theta). \tag{A 4}$$

Substituting (A 3) and (A 4) for the upward and downward propagating beams, respectively, in (A 1), it is a simple matter to show that

$$\psi_{R+}(x,z) = \psi_{R-}(x,-z), \tag{A 5}$$

from which it follows that their superposition, $\psi_R(x,z) = (\psi_{R+} + \psi_{R-})(x,z)$, is even about the positive x-axis.

In particular, at $z = 0$ the superposition evaluates to

$$\psi_R(x,0) = -iWRe^{i\Theta}\int_0^\infty \frac{J_1(K)}{K}\exp\left(-K^3\lambda\frac{x\sin\Theta}{R} + iK\frac{x\cos\Theta}{R}\right)\,dK, \quad x > 0. \tag{A 6}$$

Likewise, it follows from (A 2) and (A 5) that the superposition, ψ_L, of the two leftward propagating beams exhibit an even symmetry about the negative x-axis. Furthermore, (A 2) shows that the wave beams exhibit an odd inversion symmetry through the origin, so that in the fixed Cartesian coordinate system

$$\psi_L(-x,-z) = -\psi_R(x,z), \quad x > 0. \tag{A 7}$$

A consequence of this relation is that the superposition of the streamfunction of all four beams exhibits an odd symmetry about the z-axis.

Hereafter, the superposition of the four beams will be denoted by

$$\Psi = \psi_{\mathrm{R}} + \psi_{\mathrm{L}} \tag{A 8}$$

From the discussion above $\Psi(x,z) = \Psi(x,-z)$, and $\Psi(-x,z) = -\Psi(x,z)$, for all x and z.

Because Ψ is a continuous function that is even about the x-axis it follows immediately that its partial z-derivative is an odd function and its partial x-derivative is an even function about the x-axis. The horizontal and vertical velocity fields for the superposition of the two beams are given by $u = -\partial\Psi/\partial z$ and $w = \partial\Psi/\partial x$, respectively. Therefore u is an odd function about the x-axis and, in particular, u is identically zero on the x-axis. In other words, the horizontal velocity fields of the upward and downward propagating waves interfere destructively along this axis. The vertical velocity field, on the other hand, is an even function, indicating that the vertical velocity of the upward and downward propagating beams interfere constructively along this axis.

Symmetry arguments and linear theory may likewise be employed to show that the perturbation density field and the vertical displacement field constructively interfere along the x-axis.

Of particular interest in this paper is the structure and symmetry of the ΔN^2 and $(N^2)_t$ fields. From linear theory it can be shown that the ΔN^2 field for the superposition of the four waves is related to Ψ by

$$\Delta N^2 = \frac{-\mathrm{i}}{\omega} N^2 \frac{\partial^2 \Psi}{\partial x \partial z}. \tag{A 9}$$

(This relationship was used in (3.7) to find ΔN^2 corresponding to the right and upward propagating wave beam.)

Applying the symmetry arguments above, it is apparent that by taking the partial derivatives of Ψ with respect to both x and z yields a function that is odd about the x-axis. Thus ΔN^2 is an odd function about the x-axis. In particular, one expects in theory that $\Delta N^2(x,0) = 0$, for all x.

Because the waves are harmonic with frequency ω (for example, as (3.1) shows explicitly for the horizontal and vertical velocity fields), the $(N^2)_t$ field can be found in terms of Ψ by multiplying (A 9) by a factor $-\mathrm{i}\omega$. Thus

$$(N^2)_t = -N^2 \frac{\partial^2 \Psi}{\partial x \partial z}. \tag{A 10}$$

Thus, like ΔN^2, $(N^2)_t$ is odd about the x-axis and $(N^2)_t(x,0) = 0$, for all x.

On the basis of linear theory, we therefore predict that the $(N^2)_t$ field formed by the superposition of the upward and downward propagating wave beams (shown, for example, in figure 5) should be exactly zero where $z = 0$. As discussed in the text, experiments show that this is not the case presumably because the amplitude of the waves is so large that linear theory does not apply.

We conclude this Appendix by giving details of the coordinate transformations from which integral solutions of fields such as ΔN^2 (e.g. see (3.8)) can be determined from x and z derivatives of the streamfunction. For simplicity, we focus on the the right and upward propagating wave beam.

From the linear transformation (A 3), horizontal (x) and vertical (z) derivatives of any function $f(x,z) \to f(r,\sigma)$ can be written in (r,σ) coordinates by

$$\frac{\partial f}{\partial x} = -\cos\Theta \frac{\partial f}{\partial \sigma} + \sin\Theta \frac{\partial f}{\partial r} \tag{A 11}$$

and

$$\frac{\partial f}{\partial z} = \sin\Theta\frac{\partial f}{\partial \sigma} + \cos\Theta\frac{\partial f}{\partial r}. \tag{A 12}$$

Thus, for the right and upward propagating wave beam (using $\psi = \psi_{R+}$ to be consistent with (3.6)) the horizontal velocity field is

$$u = -\frac{\partial \psi}{\partial z} = -\sin\Theta\frac{\partial \psi}{\partial \sigma} - \cos\Theta\frac{\partial \psi}{\partial r}. \tag{A 13}$$

Indeed, unless Θ is infinitesimally small, the boundary layer approximation can be applied (Thomas & Stevenson 1972) to give $u \simeq -\sin\Theta\,\partial\psi/\partial\sigma$. Similarly, the vertical velocity field is

$$w = -\cos\Theta\frac{\partial \psi}{\partial \sigma} + \sin\Theta\frac{\partial \psi}{\partial r} \simeq -\cos\Theta\frac{\partial \psi}{\partial \sigma}. \tag{A 14}$$

Using (3.7), the ΔN^2 field for the right and upward propagating wave beam is

$$\Delta N^2 = \frac{-\mathrm{i}}{\omega}N^2\left(\frac{\partial^2\psi}{\partial r^2}\cos\Theta\sin\Theta + \frac{\partial^2\psi}{\partial r\partial\sigma}\sin^2\Theta - \frac{\partial^2\psi}{\partial\sigma\partial r}\cos^2\Theta - \frac{\partial^2\psi}{\partial\sigma^2}\sin\Theta\cos\Theta\right) \tag{A 15}$$

which, in the boundary layer approximation, is

$$\Delta N^2 \simeq \frac{\mathrm{i}}{\omega}\sin\Theta\cos\Theta N^2\frac{\partial^2\psi}{\partial\sigma^2}. \tag{A 16}$$

In practice, we apply (A 15) to equation (3.6) to get (3.8). The approximation (A 16) amounts to setting $\lambda = 0$ everywhere in (3.8) except where it appears in the exponential. The computational savings in this approximation are negligible however.

Nonetheless, it is worth commenting that in our experiments $\lambda \simeq 0.002$. Thus, discarding λ is equivalent to neglecting structures in the integrand of (3.8) with a length scale smaller than $\ell = 2\pi/k \simeq 2\pi R\sqrt{\lambda} \simeq 0.02\,\mathrm{cm}$. This is below the resolution of the experiments reported here.

REFERENCES

Appleby, J. C. & Crighton, D. G. 1986 Non-Boussinesq effects in the diffraction of internal waves from an oscillating cylinder. *Q. J. Mech. Appl. Maths* **39**, 209–231.

Appleby, J. C. & Crighton, D. G. 1987 Internal gravity waves generated by oscillations of a sphere. *J. Fluid Mech.* **183**, 439–450.

Batchelor, G. K. 1967 *An Introduction to Fluid Dynamics*. Cambridge University Press.

Bell, T. H. 1975 Lee waves in stratified flows with simple harmonic time dependence. *J. Fluid Mech.* **67**, 705–722.

Dalziel, S. B. 1992 Decay of rotating turbulence: some particle tracking experiments. *Appl. Sci. Res.* **49**, 217–244.

Dalziel, S. B., Hughes, G. O. & Sutherland, B. R. 1999 Whole field density measurements. *Exps. Fluids* (submitted).

Dvorak, V. 1880 Über eine neue einfache Art der Schlierenbeobachtung. *Ann. Phys. Chem.* **9**, 502–512.

Greenberg, P. S., Klimek, R. B. & Buchele, D. R. 1995 Quantitative rainbow schlieren deflectometry. *Appl. Optics* **34**, 3810–3822.

Hurley, D. G. 1997 The generation of internal waves by vibrating elliptic cylinders. Part 1. Inviscid solution. *J. Fluid Mech.* **351**, 105–118.

Hurley, D. G. & Keady, G. 1997 The generation of internal waves by vibrating elliptic cylinders. Part 2. Approximate viscous solution. *J. Fluid Mech.* **351**, 119–138.

Irvin, B. R. & Ross, J. 1991 Observations of pattern evolution in thermal convection with high-resolution quantitative schlieren imaging. *Phys. Fluids* A **3**, 1699–1710.

Kistovich, A. V., Neklyudov, V. I. & Chashechkin, Y. D. 1990 Nonlinear two-dimensional internal waves generated by a periodically moving source in an exponentially stratified fluid. *Izv. Atmos. Oceanic Phys.* **26**, 771–776.

Lighthill, M. J. 1978 *Waves in Fluids.* Cambridge University Press.

Mach, E. & Weltrubsky, J. von 1878 Über die Formen der Funkenwellen. *Sitzungsber. Kaiserl. Akad. Wiss Wien, Math.–Naturwiss. Kl. Abt*. 1 **78**, 551–560.

Makarov, S. A., Neklyudov, V. I. & Chashechkin, Y. D. 1990 Spatial structure of two-dimensional and monochromatic internal-wave beams in an exponentially stratified liquid. *Izv. Atmos. Oceanic Phys.* **26**, 548–554.

Merzkirch, W. 1974 *Flow Visualization.* Academic Press.

Merzkirch, W. & Peters, F. 1992 Optical visualisation of internal gravity waves in stratified fluid. *Optics and Lasers in Engng* **16**, 411–425.

Mowbray, D. E. & Rarity, B. S. H. 1967 A theoretical and experimental investigation of the phase configuration of internal waves of small amplitude in a density stratified liquid. *J. Fluid Mech.* **28**, 1–16.

Peters, F. 1985 Schlieren interferometry applied to a gravity wave in a density-stratified fluid. *Exps. Fluids* **3**, 261–269.

Press, W. H., Flannery, B. P., Teukolsky, S. A. & Vetterling, W. T. 1993 *Numerical Recipes: The Art of Scientific Computing*, 2nd Edn. Cambridge University Press.

Scheitle, H. & Wagner, S. 1990 A four colours line grid schlieren method for quantitative flow measurement. *Exps. Fluids* **9**, 333–336.

Sutherland, B. R. & Linden, P. F. 1998 Internal wave generation by flow over a thin barrier. *J. Fluid Mech.* **377**, 223–252.

Thomas, N. H. & Stevenson, T. N. 1972 A similarity solution for viscous internal waves. *J. Fluid Mech.* **54**, 495–506.

Toepler, A. 1864 *Beobachtungen nach einer neuen optischen methode*. Max Cohen u. Sohn, Bonn.

Voisin, B. 1991 Internal wave generation in uniformly stratified fluids. Part 1. Green's function and point sources. *J. Fluid Mech.* **231**, 439–480.

Weast, R. C. 1981 *Handbook of Chemistry and Physics*, 62nd Edn. CRC Press.